

**MATRIX PENCIL METHOD AS A
SIGNAL PROCESSING TECHNIQUE:
PERFORMANCE AND APPLICATION
ON POWER SYSTEM SIGNALS**

CHIA MENG HWEE

**NATIONAL UNIVERSITY OF
SINGAPORE**

2013

**MATRIX PENCIL METHOD AS A
SIGNAL PROCESSING TECHNIQUE:
PERFORMANCE AND APPLICATION
ON POWER SYSTEM SIGNALS**

CHIA MENG HWEE

(B.Eng.(Hons.), NUS)

**A THESIS SUBMITTED FOR THE DEGREE OF
MASTERS OF ENGINEERING
DEPARTMENT OF ELECTRICAL & COMPUTER
ENGINEERING
NATIONAL UNIVERSITY OF SINGAPORE**

2013

DECLARATION

I hereby declare that this thesis is my original work and it has been written by me in its entirety. I have duly acknowledged all the sources of information which have been used in the thesis.

This thesis has also not been submitted for any degree in any university previously.

Chia Meng Hwee

31 July 2013

*To my parents,
and my lovely wife, Madelyn Yeo*

Acknowledgments

When I began this project in late 2010, I have hoped that this work would be of value to the world at large. Of course, it still remains to be seen what kind of impact this would have but I hope that my labour will contribute even in any small ways to the person who reads this thesis. And thank you (yes, YOU) for taking the time to read this thesis.

This work would not have been possible with the contributions from many people whom I am deeply indebted to. Firstly, I would like to thank my wife who took care of our baby while I was shutting myself up in the room, trying to make sense out of the signals. Although she may not understand much of this thesis, I would still like to dedicate this piece of work to my lovely wife.

I would also like to thank my parents who have brought me up to become a fine person. I have always regretted not to have taken a nice graduation photograph with them during my B.Eng convocation and not have insisted on them attending my past graduation ceremony. Now I can finally do that!

Next, I would like to thank my mentor in faith, Dr. Daisaku Ikeda, whose words have kept me going on through the many months of darkness and also reminded me what on earth I am here for. That is to become the best human being I can be and create value while I am alive. Thank you Sensei.

Last but not least, I would like to thank my supervisor, A/P Ashwin M Khambadkone, who has given valuable lessons in the techniques of doing research and also critical analyses of my work that push me to think harder and go further.

Contents

List of Figures	ix
List of Tables	xii
1 Research Background and Problem Definition	1
1.1 Introduction to Signal Processing in Power Systems	1
1.1.1 Overview and Trends in Power System Analysis . .	2
1.1.2 Application Examples of Signal Processing	5
1.2 Contribution of the Thesis	9
1.2.1 Part 1: Feature Extraction Performance of Matrix Pencil Method (MPM)	9
1.2.2 Part 2: New Application of MPM	10
1.3 Organization of the Thesis	10
2 Matrix Pencil Method	12
2.1 Matrix Pencil Mathematical Formulation	12
2.1.1 MPM	12
2.2 Software Implementation of MPM in LabVIEW	16
3 Performance of MPM:Damping Factor and Frequency Es- timation	17
3.1 Current Literature on Feature Extraction Performance of MPM	17
3.2 Statistical Analysis of MPM	19
3.2.1 Feature Extraction Performance of MPM for Power System Signals	19
3.2.2 Description of the test signal	20
3.2.3 Definitions of terms	20
3.2.4 Discretized Signal and Discrete Parameters	22
3.3 Performance of MPM on Complex Exponential Signals . .	23

3.3.1	Effects of Varying the Sampling Period and Sampling Window Width	24
3.3.2	Effects of Varying the Frequency Component and Sampling Period	27
3.3.3	Effects of Varying the Damping factor and Sampling Period	30
3.3.4	Summary	32
3.3.5	Acknowledgments	34
4	Performance of MPM: Amplitude and Phase Estimation	35
4.1	Effects of Varying Sampling Frequency and Sampling Window Width	35
4.1.1	Amplitude and Phase Estimation	36
4.2	Effects of Varying the Frequency Component and Sampling Period	36
4.2.1	Amplitude and Phase Estimation	38
4.2.2	Comparison with Damping Factor and Frequency Estimates	39
4.3	Effects of Damping Factor Variation and Sampling Frequency	39
4.3.1	Amplitude and Phase Estimation	40
4.3.2	Comparison with Damping Factor and Frequency Estimates	42
4.4	Summary	43
5	Application of MPM on Subcycle Voltage Dip and Swell Classification	45
5.1	Introduction	45
5.2	Classification of Voltage Dips and Swells using Space Vector [1]	49
5.3	Application of MPM	53
5.3.1	Signals of interest	53
5.4	Choice of Sampling Frequency	55
5.4.1	Signal Processing and Classification Algorithm	57
5.4.2	Simulation of fault and Discussion	58
5.4.3	Summary of Results	62
6	Modifications to Fault Classification Algorithm	64
6.1	Simulation Setup - IEEE 34-Bus System	64
6.1.1	Results of Parameter Estimation with MPM only	65
6.1.2	Augmenting with Ellipse Fitting	67
6.1.3	Limitations of Current Method	71
6.2	Fast Implementation of Fault Classification	71

6.2.1	Simulation and Results	75
6.3	Summary of Results	79
7	Conclusion and Future Work	80
7.1	Conclusion	80
7.2	Future Work	81
	Bibliography	82

Summary

MPM has been shown to be a promising method of feature extraction signal processing method in power system analysis. This thesis analyzed the performance of MPM in greater detail and proposed a new application in sub-cycle fault signal analysis using MPM.

Signal processing holds great importance in the analysis of electrical power systems. At the start, a brief overview of present power system analysis and application examples of signal processing techniques on power system phenomena has been given. MPM is then explained in detail.

The performance of MPM in relation to sampling window width, sampling frequency and damping factor has been statistically analyzed in the first part of the thesis. For a 50 Hz signal with damping factor of less than -593.6 s^{-1} , the signal's frequency can be estimated within a variance of 1 Hz^2 with 0.1 to 1 cycle of sampled data of the signal.

In the second part of the thesis, MPM has been applied to realistic fault signals simulated in the IEEE 34-bus test system [2] to classify the fault type based on feature extraction of space vectors and zero-sequence signals. It was found that while using MPM alone was able to provide a correct fault classification using 15 ms of post-fault data, augmenting an ellipse fitting algorithm to MPM could improve the performance the fault classification to using 5 ms of post-fault data.

This classification method is computationally intensive due to the large number of samples to be processed by MPM and takes 100 ms to 300 ms to compute. Thus in order to reduce this time, a pre-filtering and down-sampling process have been added. The maximum amount of time for this improved algorithm to complete on an Intel®Core 2™Duo CPU T8300

system is 3 ms. This fast computation thus allows the dip to be classified within 9 to 10 ms from the onset of the dip. This is an improvement from the original method proposed in Vanya [1] that employed Fast-Fourier Transform (FFT) to extract the 50 Hz components as that would require a sampling window of at least 20 ms, which is one cycle of the fundamental frequency.

List of Figures

1.1	Time frame of Power System Dynamic Phenomena [3] . . .	4
3.1	a. Mean Absolute Estimate Error and b. Variance of Damping Factor Estimate for different T_s and K on Signal, $e^{(j\frac{10}{180}\pi)}e^{[-5.0+j2\pi(50)]t}$	25
3.2	a. Mean Absolute Estimate Error and b. Variance of Frequency Estimate for different T_s and K on Signal, $e^{(j\frac{10}{180}\pi)}e^{[-5.0+j2\pi(50)]t}$	26
3.3	a. Mean Absolute Estimate Error and b. Variance of Damping Factor Estimate for different sampling period, T_s and complex exponential angle, θ . Sampling Window Width, $K = 500$, and Damping Factor, $\alpha = -5.0s^{-1}$	28
3.4	a. Mean Absolute Estimate Error and b. Variance of Frequency Component Estimate for different sampling period, T_s and complex exponential angle, θ . Sampling Window Width, $K = 500$, and Damping Factor, $\alpha = -5.0s^{-1}$	29
3.5	Blown-up Plot of Variance of Damping factor Estimate for θ in the range $[-0.486\pi, -0.5\pi]$	29
3.6	a. Mean Absolute Estimate Error and b. Variance of Damping Factor Estimate for different sampling period, T_s and complex exponential angle, θ . Sampling Window Width, $K = 500$, and Frequency, $\omega = 2\pi(50.0)\text{rad s}^{-1}$	31
3.7	a. Mean Absolute Estimate Error and b. Variance of Frequency Estimate for different sampling period, T_s and complex exponential angle, θ . Sampling Window Width, $K = 500$, and Frequency, $\omega = 2\pi(50.0)\text{rad s}^{-1}$	32
3.8	Variance of Frequency Estimate for different sampling period, T_s and complex exponential angle, θ . Sampling Window Width, $K = 500$, and Frequency, $\omega = 2\pi(50.0)\text{rad s}^{-1}$.	32
4.1	a. Mean Absolute Estimate Error and b. Variance of Amplitude Estimate for different T_s and K on Signal, $1.0e^{(j\frac{10}{180}\pi)}e^{[-5.0+j2\pi(50)]t}$	37

4.2	a. Mean Absolute Estimate Error and b. Variance of Phase Angle Estimate for different T_s and K on Signal, $1.0e^{(j\frac{10}{180}\pi)}e^{[-5.0+j2\pi(50)]t}$	37
4.3	a. Mean Absolute Estimate Error and b. Variance of Amplitude Estimate for different sampling period, T_s and complex exponential angle, θ . Sampling Window Width, $K = 500$, and Damping Factor, $\alpha = -5.0s^{-1}$.	38
4.4	a. Mean Absolute Estimate Error and b. Variance of Phase Estimate for different sampling period, T_s and complex exponential angle, θ . Sampling Window Width, $K = 500$, and Damping Factor, $\alpha = -5.0s^{-1}$.	39
4.5	Variance Estimates of a. Damping Factor, b. Frequency, c. Amplitude and d. Phase Angle Estimate for different sampling period, T_s and complex exponential angle, θ . Sampling Window Width, $K = 500$, and Damping Factor, $\alpha = -5.0s^{-1}$.	40
4.6	a. Mean Absolute Estimate Error and b. Variance of Amplitude Estimate for different sampling period, T_s and complex exponential angle, θ . Sampling Window Width, $K = 500$, and Frequency, $\omega = 2\pi(50.0)\text{rad s}^{-1}$.	41
4.7	a. Mean Absolute Estimate Error and b. Variance of Phase Estimate for different sampling period, T_s and complex exponential angle, θ . Sampling Window Width, $K = 500$, and Frequency, $\omega = 2\pi(50.0)\text{rad s}^{-1}$.	42
4.8	Variance Estimates of a. Damping Factor, b. Frequency, c. Amplitude and d. Phase Angle Estimate for different sampling period, T_s and complex exponential angle, θ . Sampling Window Width, $K = 500$, and Frequency, $\omega = 2\pi(50.0)\text{rad s}^{-1}$.	43
5.1	Variance of a. Analog Angular Frequency, b. Analog Damping Factor, c. Amplitude, d. Phase Angle Estimates of Signal, $Ae^{(j\frac{10}{180}\pi)}e^{[\frac{2\pi(50)}{\tan\theta}+j2\pi(50)]t}$	56
5.2	Single Line Diagram of Simple Theoretical Case	60
5.3	Fault waveforms generated for simple case	60
5.4	Estimated SI , r_{maj} and $ V_{10} $ for Type E Dip.	61
5.5	Estimated ϕ_{inc} for Type E Dips.	62
5.6	Estimated Dip Type for (left) Type C, and (right) Type G Dips.	62
6.1	Simulated Network	66
6.2	Fault voltage waveforms and MPM measured voltages during Type C and G voltage dips.	66

6.3	Measured voltage space vector, MPM estimated fundamental frequency space vector and MPM with augmented Ellipse fitting estimate for (1) Type C and (2) Type G Dips. Segments (a) and (b) are the MPM estimation from (-5ms, 0s) and (0, 5ms) sampling windows respectively. Segment (c) is the estimated space vector extrapolated to 20 ms based on MPM's results from first 5 ms.	67
6.4	Estimated ϕ_{inc} for Type C and G Dips with and without Ellipse fitting.	68
6.5	Estimated SI and r_{maj} for Type C and G Dips with and without Ellipse fitting.	68
6.6	Estimated Dip Type for Type C and G Dips with and without Ellipse fitting.	68
6.7	Ellipse Parameters	70
6.8	Step Response of Low-Pass Butterworth Filter with cut-off frequency at 1200 Hz	73
6.9	Frequency Response of Low-Pass Butterworth Filter with cut-off frequency at 1200 Hz	74
6.10	Frequency Plot of Raw and Filtered IEEE Case G-Type Dip Space Vector Signal	74
6.11	Fault Classification Process	75
6.12	Fault voltage waveforms and MPM measured voltages during Type D and F voltage dips.	76
6.13	Measured voltage space vector, MPM estimated fundamental frequency space vector and MPM with augmented Ellipse fitting estimate for (1) Type D and (2) Type F Dips. Segments (a) and (b) are the MPM estimation from (-6ms, 0s) and (0, 6ms) sampling windows respectively. Segment (c) is the estimated space vector extrapolated to 20 ms based on MPM's results from first 6 ms.	76
6.14	Estimated ϕ_{inc} for Type D and F Dips with and without Ellipse fitting.	77
6.15	Estimated SI and r_{maj} for Type D and F Dips with and without Ellipse fitting.	77
6.16	Estimated Dip Type for Type D and F Dips with and without Ellipse fitting.	77

List of Tables

1.1	Examples of Power System Dynamic Phenomena based on Phenomena Groups	4
5.1	Dip Types' Voltage Phasors and Space Vectors (Adapted from [4, 1])	51
5.2	Classification of Voltage Dip and Swells based on Space Vector and Zero-Sequence Voltage [1]	54
5.3	Group I Classification	59
5.4	Group 2 Classification based on $ V_{10} $ and $\phi_{10} - \phi_{1+}$	60

Chapter 1

Research Background and Problem Definition

1.1 Introduction to Signal Processing in Power Systems

Signal processing holds great importance in the analysis of electrical power systems. Signal processing is often the first step in extracting useful information from the voltage and current signals. It enables the operator or control system to make sense of the signals and come to an informed control decision. As the trend towards “smart grid” accelerates, the application of advanced signal processing on power system signals becomes even more crucial. In this introduction, a brief overview of present power system analysis shall first be given. Subsequently, application examples of signal processing techniques on power system phenomena shall be highlighted to illustrate the state-of-the-art. Then a description of Matrix Pencil Method (MPM) and related methods’ application is included. Lastly, the contribution of this work to the advancement of this area shall be explained and

highlighted.

1.1.1 Overview and Trends in Power System Analysis

Conventional power systems consist of three main levels; the generation, transmission and distribution levels. Generation is conventionally made up of mainly electro-mechanical rotating inertial systems that maintains a generally constant voltage frequency of 50 Hz or 60 Hz. These generation sources are relatively large and located far away from the consumers. They are connected to the transmission networks, usually overhead lines, that transmit electrical power at high voltages over large distances to the distribution networks. At the distribution level, the voltages are stepped down to medium or low voltage levels where the power is delivered to the consumers via either overhead power lines or underground cables in densely populated urban areas. In such conventional systems, power is virtually transmitted in one direction [5]. The load demands are more or less predictable based on historical data and most of the intelligent sensing and control are done at the generation and transmission levels. There is relatively lesser need for additional intelligent control at the distribution levels other than the usual protection devices.

However, this conventional top-down system is changing. The penetration levels of renewable energy sources in the grid is already increasing throughout the world. Renewable sources such as wind and solar Photovoltaic (PV) are often connected to the power network at the distribution level via power electronic converters as Distributed Generation (DG)s. Their power production is often subjected to changing weather conditions and are thus much less controllable as compared to conventional power sources. These DGs supply power back at the distribution level and increase the difficulty in maintaining the stability and power quality of the

grid. This inadvertently increases the need for more sensing and control at the distribution level [6].

On top of this, conventional power systems also suffer from under-investment and increasing load demand. As a result, the grid has to operate at a higher load demand with an aging infrastructure [5]. Increased sensing is required to enable the operators to maximize the operating envelope with minimum disruptions by for example, predicting and locating imminent faults and maintaining the stability of the grid especially in case of power swings. These trends have all but led to a renewed interest in signal processing at all levels of the power system and especially at the distribution level.

Time scales of Power System Dynamics

For ease of analysis, power system phenomena can be broadly classified into four groups based on their time scales; namely, wave, electromagnetic, electromechanical and thermodynamic as shown in Figure 1.1 [3]. The wave group corresponds to the propagation of electromagnetic waves, for example, surge phenomena due to lightning or switching operations. The electromagnetic group refers to the electromagnetic dynamics due to for example, the interaction between the generator and the electrical network. The electromechanical group refers to the slower electromechanical dynamics for example, between rotating masses of generators and other inertial systems. The last group refers to the slowest thermodynamic changes due to for example adjustment in fuel consumption rate in a coal power plant.

As this time frame classification is highly related to type of dynamics occurring, the granularity and types of models used to analyze different classes of phenomena are not the same. The signals used are consequently different. For example, in analysis of inter-area power oscillation where

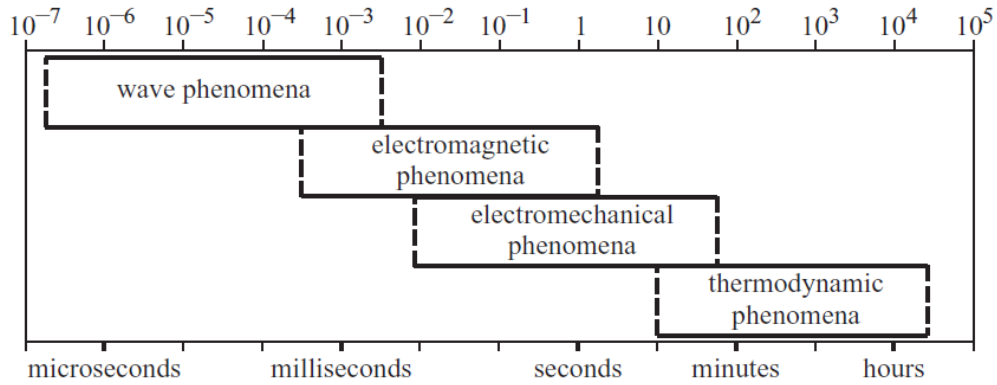


Figure 1.1: Time frame of Power System Dynamic Phenomena [3]

Table 1.1: Examples of Power System Dynamic Phenomena based on Phenomena Groups

Wave
Fault wave propagation [11, 12], Lightning surges [13]
Electromagnetic
Electromagnetic transients during faults [9, 10], Harmonic distortions [14]
Electromechanical
Inter-area power oscillations, Transient and Voltage stability [15]
Thermodynamic
Boiler turbine system [16], [17]

the electromechanical dynamics come into play, the electromagnetic voltage signals are implicitly assumed to be sinusoidal phasors albeit with “slowly” changing frequencies and amplitudes [7], [8]. Whereas in electromagnetic transient analysis for example for fault signals, instantaneous voltage and current signals are used to analyze the phenomenon [9], [10]. Detailed model of the electromechanical part of the power system is not needed in this case.

1.1.2 Application Examples of Signal Processing

There is a huge multitude of signal processing techniques that are applied in power systems and this introduction is by no means an exhaustive survey of these techniques. Instead, this thesis shall only focus on recent examples of a few related signal processing techniques to highlight the state-of-the-art for such applications on power systems.

Discrete Fourier Transform (DFT)

DFT can be said to be the most commonly used signal processing technique. A well-known fast variant of DFT is called the FFT which speeds up the processing tremendously. DFT transforms the time-domain signal into a frequency domain spectrum, thus breaking down the signal into its discrete frequency components. The main drawbacks of FFT are however, an inability to extract damping information, limitation of frequency resolution by the sampling window width, and spectral leakage. Despite these disadvantages, it is still extremely useful and popular in extracting frequency information from the data.

For example in [18] and [19], DFT has been used to measure wideband grid impedance. The knowledge of wideband grid impedance is especially important for grid-connected inverters as a mismatch between the inverter's output impedance and the grid impedance could lead to harmonic resonance [20]. In both cases, a frequency-rich current was injected by rapid electronic switching while the voltage was measured. The frequency dependent impedance was then estimated by dividing the voltage frequency spectrum by the current spectrum. Another application of DFT is the measurement of the fundamental frequency and harmonic components of space-vectors [21], [1] to estimate positive and negative sequence

components in unbalanced three-phase systems. In the analysis of wide area oscillations [22], DFT is also widely used to measure spectral signatures of low-frequency power oscillations in normal situation as well as after a disturbance event such as a fault. These signatures provide an indication of the occurrence of dynamic events in the grid.

Wavelet Transform

Wavelet Transform (WT) is another widely researched signal processing tool for power system signals in recent years. One of the most important motivations for using WT is its superior ability over DFT or Short Time Fourier Transform (STFT) to analyze non-stationary signals. It provides information about a signal in the time-frequency domain simultaneously through transformations with respect to a mother wavelet. A good introductory tutorial on this method can be found in [23]. WT uses a variable wavelet that is calculated by scaling and time-shifting a mother wavelet. This wavelet is then mathematically compared with the sampled signal through a convolution operation. Through a series of scaling and time-shifting of the mother wavelet, the time-frequency spectrum of the non-stationary signal can be found.

Due to its ability of perform multi-frequency resolution analysis, WT is used to analyze the perturbations at certain characteristic frequencies. For example, in [24], WT is used to track the changes in amplitude at the fault-characteristic frequency of the power signal of a wind turbine synchronous generator. In [25] and [26], WT is used in a similar fashion on the current signal of motor drives. A more recent development is in the use of WT in the damping estimation of electromechanical oscillations under ambient excitation conditions [27, 28]. The mode of interest is first extracted using WT, then the damping ratio is estimated using random

decrement technique.

The drawback of WT is that it is computationally intensive [29]. Furthermore, its performance is also highly dependent on the mother wavelet. Thus much testing is required to find the optimal mother wavelet for a particular application. Lastly, similar to the DFT, the highest frequency resolution is limited to the inverse of the sampling window width [23].

MPM and Prony Analysis

MPM and Prony Analysis [30] are two closely related techniques that estimate the signal as a sum of complex exponentials. The amplitudes, frequencies, phases and the damping factors are extracted as a result. However, these two methods differ in the way the signal poles (ie. the frequencies and damping factors) are extracted. Prony analysis takes a polynomial approach [31] where the poles are found as roots to a polynomial whereas MPM locates the poles by finding the eigenvalues to a matrix pencil. MPM has been shown to perform better in noise and has fewer limitations in comparison [32], [33]. Furthermore, Prony analysis sampling window length require at least one and a half times the period of frequency of interest [34] to be accurate. On the other hand, it shall be shown in latter chapters that MPM can perform relatively well even with sub-cycle sample window width.

The advantage of these two techniques over other techniques is that they are able to extract the damping factors. This is useful as it can estimate the eigenvalues of a linear system from the transient response. Furthermore, the frequency resolution is not limited to the sampling window width unlike DFT. Thus it can estimate the frequency much more accurately given a short sampling window. However, one drawback of these two techniques is their high computational requirements [14]. As a result, their uses are

often limited to offline analysis.

Prony analysis has been used in [35], [14] and [36] as a spectral technique to estimate the frequency components in voltage signals containing harmonic distortion and has been shown to perform better than DFT in terms of accuracy and frequency resolution. In [14], a filter-bank structure has been augmented with Prony analysis to reduce the computational complexity in order to speed up processing. Prony analysis and MPM has been applied respectively in [9] and [10] to fault transient signals to estimate the impedance and subsequently the fault distance. [9] extracts the phase fundamental component and DC offset components for calculation while [10] estimates the zero-sequence signals' transient dominant frequency component parameters. In wide area power system analysis applications, Prony analysis is most widely used as a “ringdown” analytical tool [22], [30]. Short bursts of disturbance test signals are injected into the system using tools such as Chief Joseph dynamic brake [37] to generate system response signals. Subsequently, modal parameters of the system are then estimated from the response signals using Prony analysis.

Summary

The above signal processing techniques are only a small section of the wide variety of techniques available. There continues to be much development in the expansion and extension of these techniques. As can be seen from the examples listed above, these techniques are not limited to one or two aspects of power system but can often be applied on a wide variety of signals across the different time scales.

This thesis provides a further extension to the body of knowledge that has been accumulated by the research community thus far. The author has found that even though MPM has been shown to be a good signal pro-

cessing method, its performance and usage has not yet been fully exploited yet in the power systems arena. Therefore this thesis shall focus on further research into this method.

1.2 Contribution of the Thesis

The contribution of this thesis can be divided into two parts.

1.2.1 Part 1: Feature Extraction Performance of MPM

An extensive evaluation of the feature extraction performance of MPM has been carried out. This study stems from the motivation to understand how MPM performs under different parameter changes such as frequency, damping factor, sampling frequency and sampling window width changes. To the best of the author's knowledge, the research literature in this aspect of MPM has been still lacking and requires a deeper research. This understanding of MPM is required to fully exploit its use as a signal processing technique for power systems area.

In this work, MPM's accuracy in extracting the amplitude, phase angle, damping factor and frequency component has been statistically analyzed using a complex exponential test signal with simulated additive white Gaussian noise. As sampling frequency and sampling window width are two important parameters that a power engineer can use to tweak the performance of MPM, multiple combinations of these two parameters were tested to find the optimal combination for a particular complex exponential signal. The exponential signals were also varied to provide insights into the selection of sampling frequency and window width. This thesis has thus provided the reader a deeper understanding of the performance of MPM on exponential signals and also a method to choose the optimal

sampling frequency and window width for a particular set of signals.

1.2.2 Part 2: New Application of MPM

Based on the study in Part 1, a new application of MPM on sub-cycle fault classification has been proposed and discussed. This new application makes use of MPM's sub-cycle feature extraction capability to elucidate the fundamental frequency component in highly distorted signals. MPM is able to estimate the frequency component of a space vector using less than half a cycle of data. The sampling frequency and window width has been chosen based on Part 1 of the work. This is in comparison with DFT techniques that usually will require at least a fundamental cycle length of data. As this technique can extract the required parameters using a much shorter sampling window width, it can potentially allow faster evaluation and subsequent control action to mitigate faults.

MPM and its close cousin, Prony Analysis require long computational time with increased number of samples and hence, are often deployed only in offline analysis. In this work, a pre-filtering and down-sampling procedure has been introduced to reduce the computation time drastically. This reduced the computation time of the algorithm to 3 ms. In total, the improved algorithm can classify the dip within 9 ms to 10 ms from the onset of the fault. This is an improvement over the Vanya's [1] method of using DFT that required at least a 20-ms sampling window. This shall be discussed in detail in Chapter 6.

1.3 Organization of the Thesis

The thesis is organized as follows:

- **Chapter 1** introduces the dynamic modeling techniques of power

systems research in terms of time scales and the uses of signal processing in these areas. The application, advantages and disadvantages of relevant signal processing techniques are also discussed in this chapter.

- **Chapter 2** describes the mathematical formulation of MPM in detail and how it can be used to extract damped complex exponential parameters.
- **Chapter 3** elaborates on the statistical analysis of MPM technique on a variable complex damped exponential signal with additive noise. In this chapter, the feature extraction performance of MPM on damping factor and frequency component is examined.
- **Chapter 4** evaluates the feature extraction performance of MPM on amplitude and phase components of the complex exponential signal.
- **Chapter 5** describes a new application of MPM on sub-cycle fault classification based on the findings from Chapter 3 and 4. This method is tested on a simple case as a start. MPM is used to process the space vectors and zero-sequence voltages of a fault signal to extract the desired parameters in order to classify the dip with only a quarter-cycle of a 50 Hz data.
- **Chapter 6** describes the testing of the method in Chapter 5 on a IEEE 34-bus test case. An ellipse fitting algorithm has been augmented to enhance the accuracy of the method consistently. A pre-filtering and down-sampling process is then employed to reduce the algorithm's computational time from 300 ms to a maximum of 3 ms.
- **Chapter 7** discusses the final conclusions of this thesis and possible future work in this area.

Chapter 2

Matrix Pencil Method

2.1 Matrix Pencil Mathematical Formulation

2.1.1 MPM

This section describes the MPM [31] in detail. MPM is a signal processing method that approximates the analog signal, $y(t)$ by a sum of M damped complex exponentials. This is expressed in Equation 2.1.

$$y(t) \approx \sum_{i=1}^M A_i e^{j\phi_i} e^{(\alpha_i + j\omega_i)t} \quad (2.1)$$

Equation 2.2 expresses the sampled case in which the time variable, t is replaced by nT_s where n represents the sample number and T_s represents the sampling period:

$$\begin{aligned} y(nT_s) = y(n) &\approx \sum_{i=1}^M A_i e^{j\phi_i} e^{(\alpha_i + j\omega_i)nT_s} \\ &= \sum_{i=1}^M A_i e^{j\phi_i} z_i^n \\ &(n = 0, \dots, N - 1) \end{aligned} \quad (2.2)$$

where $y(n)$ = Measured Discrete Signal,

A_i = Amplitudes of i th component,

ϕ_i = Phase Angle of i th component,

α_i = Damping factor of i th component,

ω_i = Angular frequency of the i th component ($\omega_i = 2\pi f_i$) where f_i is the frequency in Hz,

$z_i = e^{(\alpha_i + j\omega_i)T_s}$ for $i = 1, 2, \dots, M$

N = Number of samples.

MPM finds the estimates for the values of A_i 's, ϕ_i 's and z_i 's from the measured data $y(n)$. It does this by a two step process. First, it finds the poles z_i 's as the solution of a generalized eigenvalue problem by using a mathematical entity known as the matrix pencil. This matrix pencil is formed using the sampled values of $y(t)$. In the second step, it then uses the new found poles to estimate the complex amplitudes, A_i 's and phase angles, ϕ_i 's by solving a least squares problem.

A matrix pencil, \mathbf{X} is a mathematical entity that is defined as the combination of two matrices, \mathbf{Y}_1 and \mathbf{Y}_2 with a scalar parameter, λ where $\mathbf{X} = \mathbf{Y}_2 - \lambda\mathbf{Y}_1$. For a discrete signal of length N , $y(n)$, we can define two $(N - L) \times L$ matrices \mathbf{Y}_1 and \mathbf{Y}_2 , as the following:

$$\mathbf{Y}_1 = \begin{bmatrix} y(0) & y(1) & \cdots & y(L-1) \\ y(1) & y(2) & \cdots & y(L) \\ \vdots & \vdots & & \vdots \\ y(N-L-1) & y(N-L) & \cdots & y(N-2) \end{bmatrix}_{(N-L) \times L} \quad (2.3)$$

and

$$\mathbf{Y}_2 = \begin{bmatrix} y(1) & y(2) & \cdots & y(L) \\ y(2) & y(3) & \cdots & y(L+1) \\ \vdots & \vdots & & \vdots \\ y(N-L) & y(N-L+1) & \cdots & y(N-1) \end{bmatrix}_{(N-L) \times L} \quad (2.4)$$

where L is an integer known as the pencil parameter that can be set arbitrarily. It has been shown that $N/3$ and $2N/3$ are the best choices for L where MPM is the least sensitive to noise [32]. Consequently, L has been set as $\text{floor}(N/3)$ so that it is close to the optimal value.

In the noiseless case, the parameters of the complex exponentials, $e^{(\alpha_i + j\omega_i)T_s}$ can be found as the generalized eigenvalues of the matrix pencil, $\mathbf{Y}_2 - \lambda\mathbf{Y}_1$ [31]. In the presence of noise however, Singular Value Decomposition (SVD) is used to pre-filter the matrices first before solving for the eigenvalues [31]. This SVD operation estimates the order, M of the signal $y(n)$. The SVD process is explained in the latter paragraphs.

The matrix \mathbf{Y} is first constructed as shown in Equation 2.5 using the sampled values of $y(n)$.

$$\mathbf{Y} = \begin{bmatrix} y(0) & y(1) & \cdots & y(L) \\ y(1) & y(2) & \cdots & y(L+1) \\ \vdots & \vdots & & \vdots \\ y(N-L-1) & y(N-L) & \cdots & y(N-1) \end{bmatrix}_{(N-L) \times L+1} \quad (2.5)$$

Then we take the SVD of \mathbf{Y} :

$$\mathbf{Y} = \mathbf{U} \mathbf{S} \mathbf{V}^* \quad (2.6)$$

where \mathbf{U} is an $(N-L) \times (N-L)$ real or complex unitary matrix, \mathbf{S} is an $(N-L) \times (L+1)$ rectangular diagonal matrix with nonnegative real numbers on the diagonal, and \mathbf{V}^* (the conjugate transpose of \mathbf{V}) is an

$(L + 1) \times (L + 1)$ real or complex unitary matrix. The individual columns of \mathbf{U} and \mathbf{V} are known as the left-singular vectors and right-singular vectors respectively while the diagonal entries of \mathbf{S} are known as the singular values of \mathbf{Y} . The order, M of the underlying signal $y(t)$ can be estimated from the rank of the matrix \mathbf{Y} provided that $M \leq L \leq N - M$ [31]. In addition, if \mathbf{Y} has rank M , then we can expect the last $L + 1 - M$ singular values in \mathbf{S} to be very close to zero [38], provided the singular values are arranged from largest to smallest.

The order M is thus estimated and the filtered matrices built with the following steps [31]. Using a noise tolerance setting, tol , the individual singular values, σ_i , are compared with the largest singular value, σ_{max} . If $(\sigma_i/\sigma_{max}) > tol$, the corresponding right singular vector in \mathbf{V} will be kept to form the filtered matrix $\mathbf{V}_{filtered}$. Otherwise, the corresponding right singular vector shall be removed. In [31], tol was set to 10^{-3} when the data was accurate up to 3 significant digits.

With M number of poles present in the signal, $\mathbf{V}_{filtered} = [v_1 v_2 \cdots v_M]$ where v_i 's are the corresponding column vectors of \mathbf{V} . Subsequently, matrices \mathbf{V}_1 and \mathbf{V}_2 are formed by removing the last row of $\mathbf{V}_{filtered}$ and the first row of $\mathbf{V}_{filtered}$ respectively. It can be shown that the eigenvalues, z_i 's of the matrix pencil $\mathbf{Y}_2 - \lambda\mathbf{Y}_1$ can be estimated by the those of $\mathbf{V}_1^+\mathbf{V}_2$ where \mathbf{V}_1^+ is the Moore-Penrose pseudo-inverse of \mathbf{V}_1 . The damping factors, α_i 's and angular frequencies, ω_i 's are then determined from z_i 's given that the sampling period is T_s .

With the eigenvalues found, the amplitudes, A_i 's, and phase angles, ϕ_i 's are then found by solving the least squares problem as shown in Equation

2.7:

$$\begin{bmatrix} y(0) \\ y(1) \\ \vdots \\ y(N-1) \end{bmatrix} = \begin{bmatrix} 1 & 1 & \cdots & 1 \\ z_1 & z_2 & \cdots & z_M \\ \vdots & \vdots & & \vdots \\ z_1^{(N-1)} & z_2^{(N-1)} & \cdots & z_M^{(N-1)} \end{bmatrix} \begin{bmatrix} R_0 \\ R_1 \\ \vdots \\ R_M \end{bmatrix} \quad (2.7)$$

where $z_i = e^{(\alpha_i + j\omega_i)T_s}$, and $R_i = A_i e^{j\phi_i}$.

2.2 Software Implementation of MPM in LabVIEW

The MPM has been fully implemented in LabVIEW [39] according to the steps described in the previous section. Even though a MPM implementation is available in LabVIEW as a software package, the reader should note that this has not been used because it can only process real input values, and not complex values as needed in our project. Secondly, developing our own implementation gives us greater flexibility and clarity in the algorithms deployed in the program.

Our implementation has been built with standard array manipulation and Linear Algebra methods such as SVD, matrix inverse method and eigenvalue method. These methods are available in the base package of LabVIEW and hence, no additional software packages have been employed.

Chapter 3

Performance of MPM:Damping Factor and Frequency Estimation

It is important to know the estimation performance of MPM in order to fully exploit its capability in terms of processing power system signals. There are research literature about evaluating the performance of MPM as a signal processing technique [32], [40], [41]. These important results will be highlighted in the following sections briefly. This project's contribution is however on the further extension of these results with the focus of using MPM on power system signals.

3.1 Current Literature on Feature Extraction Performance of MPM

MPM is a powerful method to extract complex exponential parameters from the signals and its performance has been favorably compared to other

methods such as Prony method [42] and FFT [40]. One important performance criteria is that of frequency resolution. José [40] evaluated how well MPM is able to resolve two closely spaced undamped sinusoidal signals. Total Forward-Backward Matrix Pencil (TFBMPM), which is a variant of MPM, has been used instead of the direct MPM method described in Chapter 2, in order to improve the performance as TFBMPM is more applicable on undamped sinusoids. Details of TFBMPM can be found in [40]. The simulation input data in [40] consisted of two complex undamped sinusoids of equal power with varying white Gaussian noise; one sinusoid was of frequency 0.2Hz and the other was varied between 0.270Hz and 0.290Hz with different phases. The observation interval was 8-sample long with a sampling period of 1 second. The variance of the frequency estimate was numerically computed after several iterations of the simulation.

The main conclusions from [40] were as follows:

The phase difference between the signals influences the frequency resolution of MPM strongly as expressed in Equation 3.1. The variance of the frequencies estimates reaches a minimum if

$$(\omega_m - \omega_n)(N - 1)T_s + 2(\theta_m - \theta_n) = (2k)\pi \quad (3.1)$$

and a maximum if

$$(\omega_m - \omega_n)(N - 1)T_s + 2(\theta_m - \theta_n) = k\pi \quad (3.2)$$

where k is an integer. The two signals used were defined as $A_m e^{j\phi_m} e^{j\omega_m t}$ and $A_n e^{j\phi_n} e^{j\omega_n t}$. The number of samples, $N = 8$ and the sampling period, $T_s = 1$ s.

MPM's frequency resolution is the worst when the frequency difference, $(\omega_m - \omega_n)$, is small and phase difference, $(\theta_m - \theta_n)$, is close to $C \times 90^\circ$ where C is an integer. It performs the best when the phase difference, $(\theta_m - \theta_n)$, is close to $C \times 180^\circ$.

In another work, El-Hadi [41] analyzed the MPM's estimation of damping factor on damped complex exponential signals with respect to L -parameter. It was found that the variance of the damping factor estimates was minimized when L -parameter = $N/3$ or $2N/3$. This result was similar to that for TFBMPM for estimating the angular frequency, ω_i in [32].

Even though the above works did provide important insights into the estimation limits of MPM, it would be beneficial to explore further into how variation in sampling frequency and sampling window width can help us optimize the performance of MPM in analyzing power system signals. To the author's knowledge, there have not yet been such studies yet, which explains the motivation for the current and next chapter. These two chapters shall evaluate the feature extraction performance of MPM with variation in sampling frequency and sampling window width.

3.2 Statistical Analysis of MPM

3.2.1 Feature Extraction Performance of MPM for Power System Signals

In power systems, we often have to measure and process voltage and current signals. A typical instantaneous voltage or current signal profile consists of a strong fundamental frequency component of 50 Hz or 60 Hz, with some harmonic components normally in the range of about 0-5%. Commercial power quality analyzers often can measure frequency components up to the 50th harmonic (about 2500 Hz or 3000 Hz) as a norm. There are also possible interharmonic, and transient components. Hence, it would be interesting to evaluate how MPM can effectively elucidate the parameters from such signals.

Among the various parameters, sampling frequency and sampling window width are the most accessible parameters that the power engineer have at hand to tweak the performance of MPM. High sampling frequency however often results in costlier data acquisition equipment and produces prodigious amount of data within a short sampling time. Processing of excessively huge amount of data adds to the processing time and computing power and thus may not be desirable. On the other hand, sampling window width determines the time length of signal information needed to be processed before the parameters can be estimated. If a long length of signal is needed, then that would invariably increase the time needed to estimate the required parameter. This again may not be desirable. Thus, an optimal sampling rate and length is required.

3.2.2 Description of the test signal

In order to analyze the effects of sampling frequency and sampling length on MPM, a statistical analysis of the performance of MPM has been carried out. A complex exponential signal of the following form has been simulated as a base case test signal:

$$Ae^{j\phi}e^{(-\alpha+j\omega)t} = 1.0 e^{j\frac{10}{180}\pi}e^{[-5.0+j2\pi(50)]t} \quad (3.3)$$

In addition, Complex Gaussian White Noise (CGWN) of variance, $\sigma^2 = 0.01$, was generated and added to the signal to simulate a noised signal. These signals were simulated and processed using MPM in Labview [39]. MPM's performance in extracting the parameters is then evaluated.

3.2.3 Definitions of terms

Analysis was carried out on the results obtained after varying the sampling period, T_s and number of samples, K . For each parameter change,

a statistical sample size of five hundred simulations were carried out to estimate the mean and variance of the results of MPM. by comparing the result with the true value that was simulated.

Using a fairly large number of statistical samples (five hundred in our case), the estimate of the required parameter from MPM can be approximated to have a normal distribution according to the Central Limit Theorem [43] as expressed in Equation 3.4.

$$\frac{1}{n} \sum_{i=1}^n \chi_i \sim N\left(\mu, \frac{\sigma^2}{n}\right) \quad (3.4)$$

where χ_i represents the i^{th} parameter estimate statistical sample using MPM, n is the number of statistical samples, μ is the estimate's mean and σ^2 is the variance of the estimate.

The mean, μ can be estimated by the sample mean, $\bar{\chi} \equiv \frac{1}{n} \sum_{i=1}^n \chi_i$, while the variance, σ^2 can be estimated by the sample variance estimate, $s_\chi^2 \equiv \frac{1}{n-1} \sum_{i=1}^n [\chi_i - \bar{\chi}]^2$.

Test signal is defined as $Ae^{(j\phi)}e^{(\alpha+j\omega)t}$ [p.u.]. The parameters that are of interest to be extracted by MPM are:

Test signal Complex Amplitude $\equiv A$ [p.u.]

Test signal Phase Angle $\equiv \phi$ [rad]

Test signal Frequency $\equiv \omega$ [rad s⁻¹]

Test signal Damping factor $\equiv \alpha$ [s⁻¹]

In addition, other symbols are defined as:

Test signal Complex Exponential angle, $\theta \equiv \tan^{-1} \frac{\omega}{\alpha}$ [rad]

Time constant of signal, $\tau \equiv \left|\frac{1}{\alpha}\right|$ [s]

Number of samples (ie. sampling window width) $\equiv K$

Number of simulations (ie. number of statistical samples) $\equiv n$

Parameter Estimate Actual Mean, μ_χ where the parameter is χ .

Mean Estimate, $\bar{\chi} \equiv \frac{1}{n} \sum_{i=1}^n \chi_i$ where the parameter is χ .

Parameter Estimate Actual Variance, σ_χ^2 where the parameter is χ .

Variance Estimate, $s_\chi^2 \equiv \frac{1}{n-1} \sum_{i=1}^n [\chi_i - \bar{\chi}]^2$ where the parameter is χ .

Parameter Estimate error, $\Delta_\chi \equiv \bar{\chi} - \chi$

3.2.4 Discretized Signal and Discrete Parameters

The process of sampling discretizes the analog signal. It would be useful to use the discrete parameters to generalize the results because, for example, a high frequency analog signal with high sampling frequency can yield the same discrete samples as a low frequency analog signal with a low sampling frequency. Let's take for example two analog signals, Signal 1: $Ae^{j\phi}e^{(\alpha_1+j\omega_1)t}$ and Signal 2: $Ae^{j\phi}e^{(\alpha_2+j\omega_2)t}$, given that $(\alpha_2 + j\omega_2) = \delta.(\alpha_1 + j\omega_1)$ where δ is a constant multiplier factor. If we sample the Signal 1 with a sampling frequency of T_s and Signal 2 with $\frac{T_s}{\delta}$, then their discrete damping factors and frequencies will be equal as shown in Equation 3.5.

$$\begin{aligned}
 \text{Signal 1 : } Ae^{j\phi}e^{(\alpha_1+j\omega_1)t} &= Ae^{j\phi}e^{(\alpha_1+j\omega_1)T_s k} \\
 &= Ae^{j\phi}e^{(\alpha_N+j\omega_N)k} \\
 \text{Signal 2 : } Ae^{j\phi}e^{(\alpha_2+j\omega_2)t} &= Ae^{j\phi}e^{\delta.(\alpha_1+j\omega_1)\frac{T_s}{\delta}k} \\
 &= Ae^{j\phi}e^{(\alpha_N+j\omega_N)k}
 \end{aligned} \tag{3.5}$$

where k is the discrete time index of the sampled signal, α_N and ω_N are the discrete damping factor and frequency respectively.

The discrete parameters are thus defined as follows:

Discrete damping factor, $\alpha_N \equiv \alpha.T_s$

Discrete angular frequency, $\omega_N \equiv \omega.T_s$ [rad]

With these relationships, it is known from statistical theory that the parameter variances are then related as shown below:

Discrete damping factor variance, $\sigma_{\alpha_N}^2 \equiv \sigma_{\alpha}^2.T_s^2$

Discrete angular frequency variance, $\sigma_{\omega_N}^2 \equiv \sigma_{\omega}^2.T_s^2$ [rad²]

In addition, the errors in estimation can be defined as:

Discrete damping factor error, $\Delta_{\alpha_N} \equiv (\bar{\alpha} - \alpha).T_s$

Discrete angular frequency error, $\Delta_{\omega_N} \equiv (\bar{\omega} - \omega).T_s$

3.3 Performance of MPM on Complex Exponential Signals

This section attempts to assess MPM's performance by varying the sampling period and the sampling window width. In addition, its performance on complex exponential signals with different ratios of damping factor and frequency is also evaluated.

The reader should note that even though a specific analog signal has been simulated, the results are shown in discrete parameters so that they can be applied to a more general set of sampled complex damped exponential signals with appropriate mathematical manipulation.

3.3.1 Effects of Varying the Sampling Period and Sampling Window Width

In order to assess the effects of sampling period, T_s and sampling window width, K on the performance of MPM, MPM was employed to extract the damping and frequency components of the signal given in subsection 3.2.2 with CGWN added as described. The signal is shown here for the convenience of the reader.

$$\text{Signal: } Ae^{j\phi}e^{(-\alpha+j\omega)t} = 1.0 e^{j\frac{10}{180}\pi} e^{[-5.0+j2\pi(50)]t}$$

T_s was varied between 0.01 s and 1 μ s while K was varied between 10 and 500. For each T_s and K change, five hundred simulations were carried out to estimate the error and variance of the damping factor and frequency estimates.

Damping Factor, α , Estimate

The results for the damping factor estimate error and variance are plotted in Figure 3.1. For this test signal, the damping factor estimate variance is the least in the dark blue region where $K \approx 500$ and the discrete damping factor, α_N , is about $-10^{-2.4} = -0.004$ as shown in Figure 3.1b. ($\alpha_N = \alpha T_s$). The mean absolute estimate error is also the least in the same region as shown in Figure 3.1a. Thus the optimal sampling period, T_s can be found by:

$$\begin{aligned} T_s = \frac{\alpha_N}{\alpha} &\approx 0.004\tau \\ \text{or } &= 800 \mu\text{s} \end{aligned} \tag{3.6}$$

where τ is the time constant of the signal as defined in Subsection 3.2.3. The sampling window width, K , should be chosen as large as possible as it can be observed that as K gets larger, the variance improves for each sampling period. However, it should also be noted that larger K

will increase the computational time required to do MPM. It can also be observed that the variance is larger in the orange region when the sampling period, T_s , is small or in other words, when the sampling frequency is high. Hence, a high sampling frequency does not necessarily lead to a good estimation result but instead, an optimal sampling frequency has to be chosen for a particular sampling window width, K . An explanation for this may be that as the sampling frequency increases for the same K , the number of cycles of the sinusoid captured reduces. Hence, after the optimal sampling frequency, the estimation of the frequency and damping factor worsens.

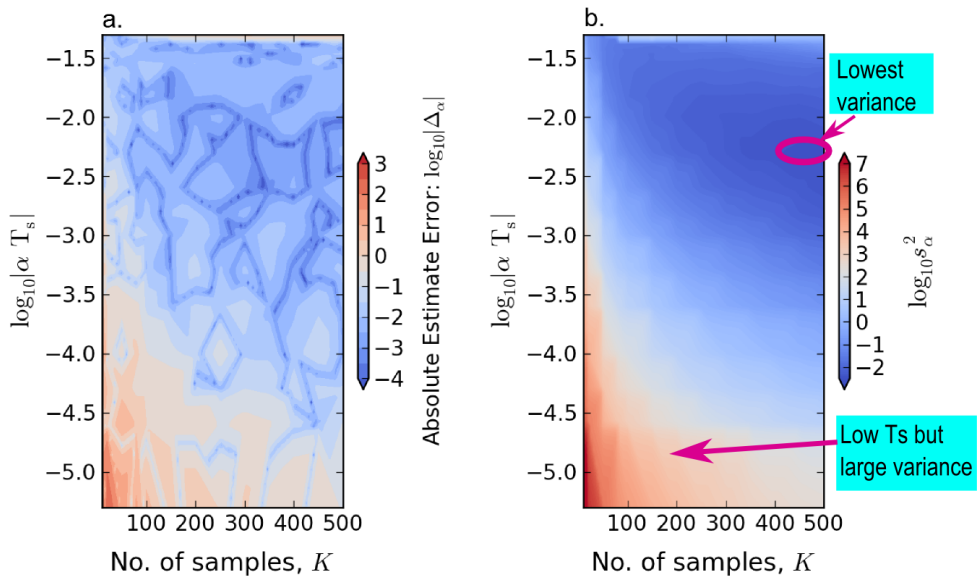


Figure 3.1: a. Mean Absolute Estimate Error and b. Variance of Damping Factor Estimate for different T_s and K on Signal, $e^{(j\frac{10}{180}\pi)}e^{[-5.0+j2\pi(50)]t}$

Angular Frequency, ω , Estimate

A similar plot has been done for the angular frequency estimate as shown in Figure 3.2. It shows similar results to the damping factor estimate

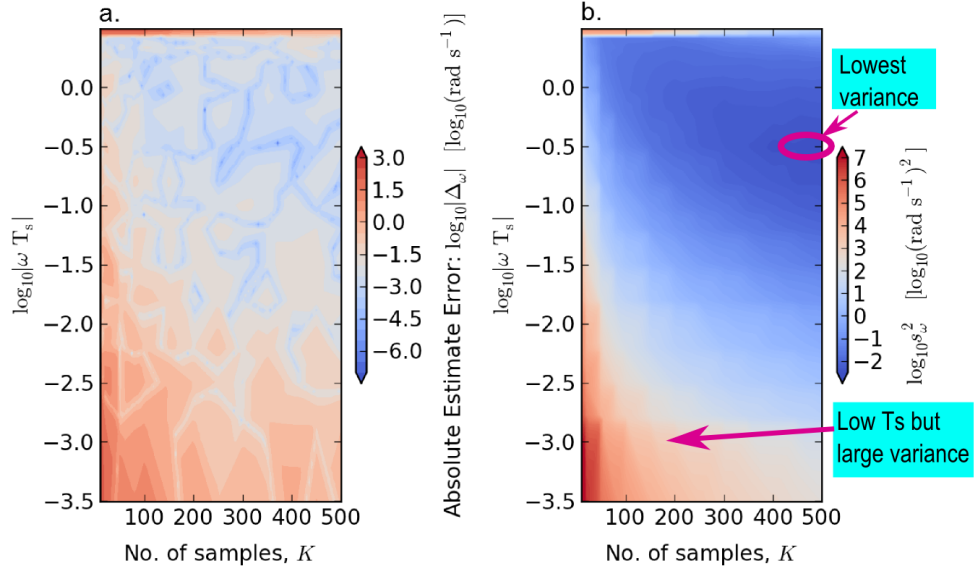


Figure 3.2: a. Mean Absolute Estimate Error and b. Variance of Frequency Estimate for different T_s and K on Signal, $e^{(j\frac{10}{180}\pi)}e^{[-5.0+j2\pi(50)]t}$

plot. The variance reduces as the sampling window width, K , increases as shown in Figure 3.2b. The variance is also similarly larger in the orange region when the sampling period, T_s , is small.

The frequency estimate variance is the least in the dark blue region where $K \approx 500$ and the discrete angular frequency, ω_N , is about $10^{-0.6} = 0.251$ rad as shown in Figure 3.2b. ($\omega_N = \omega T_s$). The mean absolute estimate error is less than $10^{-1.5}$ rad s^{-1} in the same region as shown in Figure 3.2a. Thus the optimal sampling period for estimating the frequency when $K=500$ can be found by:

$$T_s = \frac{\omega_N}{\omega} \approx \frac{0.251}{2\pi(50)} = 0.0008s \quad (3.7)$$

or = 0.04 of frequency component period

From these results, we can observe that a large sampling window width, K , would give a good estimate of the damping factor and frequency of a particular damped complex exponential signal. This result is intuitive as

a large sampling window will inevitably cover a longer length of the signal and thus provide a more accurate estimate. In addition, for a given window width, K , an optimal sampling frequency can be found from the statistical results.

In comparison, for DFT which is a common signal processing technique, a larger K increases the frequency resolution of the estimate. The frequency resolution can be calculated as follows:

$$\text{Frequency Resolution [Hz]} = \frac{1}{2T_s} \cdot \frac{1}{K} \quad (3.8)$$

Using the sampling frequency of $T_s = 0.0008\text{s}$ and $K = 500$ obtained earlier for MPM, the frequency resolution of DFT is 1.25 Hz. On the other hand, for the same sampling frequency and sampling window width, MPM's frequency estimate's variance is 10^{-4} Hz^2 , or in other words, a standard deviation of 0.01 Hz. For a confidence level of 99.99%, the confidence interval is about six times the standard deviation or 0.06 Hz. Hence, MPM gives a better resolution to the frequency than DFT with equal sampling frequency and window width.

3.3.2 Effects of Varying the Frequency Component and Sampling Period

Since we have found that large K gives a better estimate in Subsection 3.3.1, K is set at a constant of 500 for the analysis in this subsection. In this subsection, the signal frequency, ω and the sampling period, T_s are varied while setting the rest of the parameters at a constant. The objective is to assess the effect of varying the frequency, ω , on the optimal sampling frequency, for the same damping factor, α . As mentioned earlier, sampling window width, K , is set at a constant 500 and damping factor, α at -5.0 s^{-1} . The complex exponential angle, θ , defined earlier in Subsection 3.2.3,

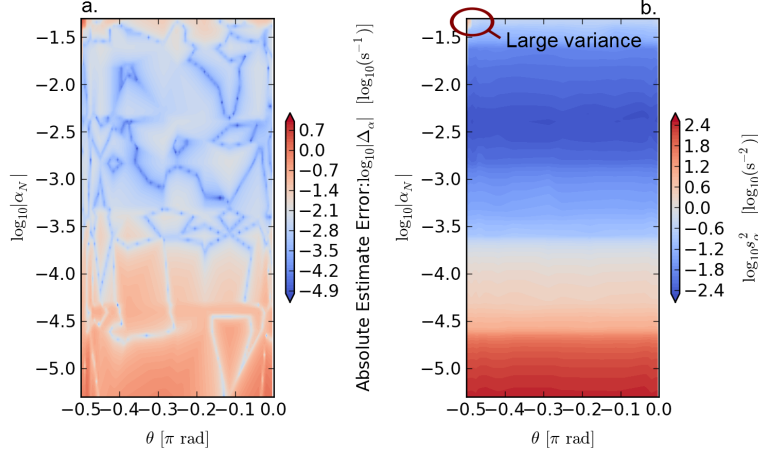


Figure 3.3: a. Mean Absolute Estimate Error and b. Variance of Damping Factor Estimate for different sampling period, T_s and complex exponential angle, θ . Sampling Window Width, $K = 500$, and Damping Factor, $\alpha = -5.0\text{s}^{-1}$.

was calculated and plotted against the discrete damping factor, α_N . The frequency component was swept from 0.01 Hz to 3000 Hz. The sampling period was varied from $1 \mu\text{s}$ to 0.01 s. The results are shown in Figure 3.3 and 3.4.

The results show that as the complex exponential angle, θ changes from 0 to $-\frac{\pi}{2}$ rad, the estimate variances of damping factor and frequency component remain quite similar for each sampling period. As shown in Figure 3.3, the variance remains at a minimum when $\alpha_N \approx -10^{-2.4}$ for θ in the range $(-\frac{\pi}{2}, 0)$. This value is very close to the one estimated in Subsection 3.3.1. Hence, for $K=500$ and a fixed α of -5.0 s^{-1} , the optimal sampling frequency occurs at 1250 Hz ($T_s = 800 \mu\text{s}$) and is minimally affected by the variation in frequency component. This shows a strength of MPM as it can estimate a range of frequencies well given the same sampling frequency.

A sudden increase in both estimate variances can be observed in the

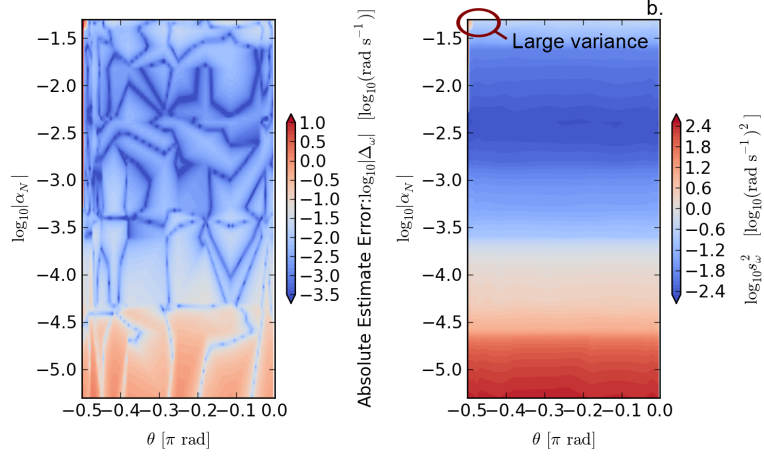


Figure 3.4: a. Mean Absolute Estimate Error and b. Variance of Frequency Component Estimate for different sampling period, T_s and complex exponential angle, θ . Sampling Window Width, $K = 500$, and Damping Factor, $\alpha = -5.0\text{s}^{-1}$.

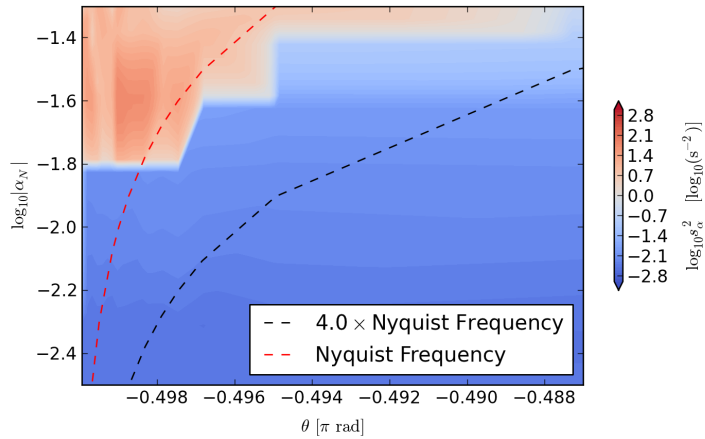


Figure 3.5: Blown-up Plot of Variance of Damping factor Estimate for θ in the range $[-0.486\pi, -0.5\pi]$

circled areas in Figure 3.3 and 3.4 when θ is close to $-\frac{\pi}{2}$. In this region, the frequency component becomes much larger relative to the damping factor. A blown-up plot for damping factor variance is shown in Figure 3.5. As the frequency component becomes large, the damping factor estimate variance increases. It can be observed that the sampling frequency becomes close to the Nyquist sampling frequency of the frequency component as shown by the dashed red line in Figure 3.5.

It can be seen in Figure 3.5 that if the sampling frequency remains above approximately 4.0 times the Nyquist frequency, then the damping factor estimation performance will be similar to that when θ is away from $-\frac{\pi}{2}$. This corresponds to the area below the blue dashed line. In other words, the sampling frequency should be set at least 4.0 times the Nyquist frequency to have a good damping factor and frequency component estimation.

3.3.3 Effects of Varying the Damping factor and Sampling Period

In this subsection, the signal damping factor, α , and the sampling period, T_s , are now varied while keeping the other parameters constant. The objective is now to assess the effect of varying the damping factor, α , on the optimal sampling frequency, for the same angular frequency, ω . Similar to the previous subsection, the damping factor and frequency estimation performance is again assessed. The sampling window width, K , was set at a constant of 500 while the angular frequency, ω was set at a constant of $2\pi(50.0)$ rad s⁻¹. The damping factor was swept from -0.01 s⁻¹ to $-50,000$ s⁻¹. This is equivalent to varying the exponential angle, θ , from -6.3×10^{-3} rad to almost -0.5π rad. The sampling period was varied from $1 \mu\text{s}$ to 0.01 s.

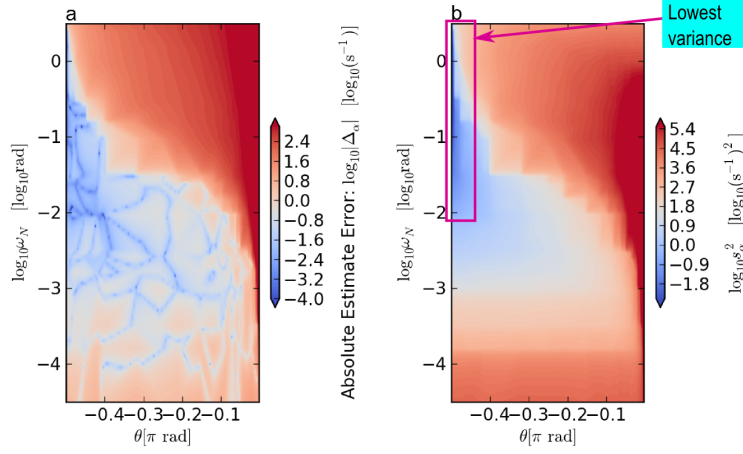


Figure 3.6: a. Mean Absolute Estimate Error and b. Variance of Damping Factor Estimate for different sampling period, T_s and complex exponential angle, θ . Sampling Window Width, $K = 500$, and Frequency, $\omega = 2\pi(50.0)\text{rad s}^{-1}$.

The complex exponential angle, θ was plotted against ω_N in Figure 3.6 and 3.7. The estimate variance and the absolute error are the lowest when θ is close to -0.5π rad and ω_N is approximately between 1 and 0.01 rad as marked out in the figures. This meant that frequency and damping factor estimates are the most accurate when signal is lightly damped.

In order to estimate the optimal sampling frequency for a signal with a particular $\omega : \alpha$ ratio, one can mark out the points with the lowest variance as shown by blue dashed line in Figure 3.8. It can also be observed that the optimal sampling period decreases as θ becomes closer to zero or in other words when the signal is highly damped. As the signal becomes highly damped, the estimate variance increases. For extremely high damping factors, MPM is not able to estimate the damping factor nor the frequency component well. One possible reason for this is that with a high damping factor, the signal is quickly attenuated and much lesser useful information can be processed by MPM.

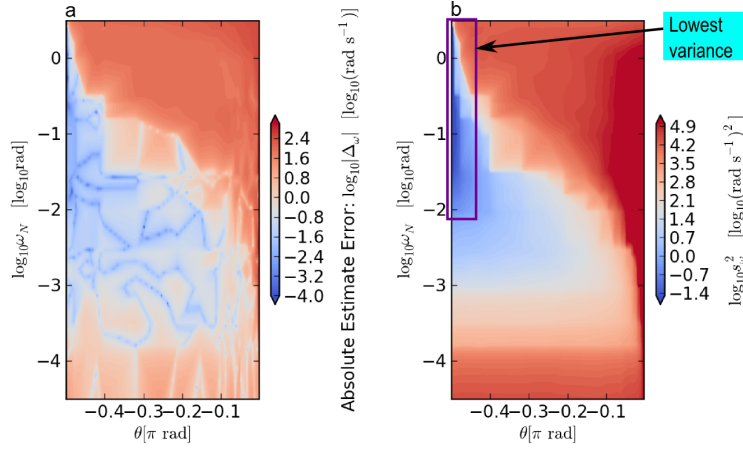


Figure 3.7: a. Mean Absolute Estimate Error and b. Variance of Frequency Estimate for different sampling period, T_s and complex exponential angle, θ . Sampling Window Width, $K = 500$, and Frequency, $\omega = 2\pi(50.0)\text{rad s}^{-1}$.

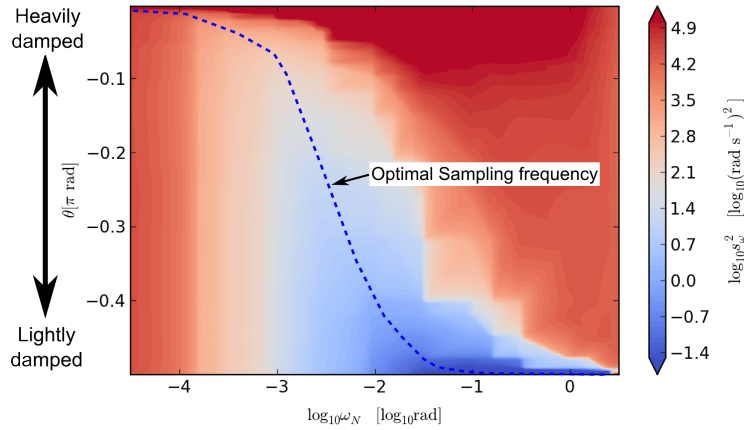


Figure 3.8: Variance of Frequency Estimate for different sampling period, T_s and complex exponential angle, θ . Sampling Window Width, $K = 500$, and Frequency, $\omega = 2\pi(50.0)\text{rad s}^{-1}$.

3.3.4 Summary

In summary, the following are the useful pointers after the statistical analysis of the damping factor and frequency.

- In general, the estimate variances reduce as the number of samples, K , increases. Thus a large K would be desirable for higher accuracy. In comparison with DFT, a larger K increases the resolution of the frequency estimation using DFT. In addition, MPM gives a better frequency resolution than DFT given the same sampling frequency and window width as described earlier in the chapter. DFT is not able to estimate the damping factor of the signal.
- It is found that for a fixed sampling window of $K=500$ and constant damping factor, the MPM estimate performance is minimally affected by changes in the frequency component. This shows a strength of MPM as it can estimate a range of frequencies well given the same sampling frequency. In addition, the sampling frequency should be set to at least about four times the Nyquist sampling frequency of the frequency component.
- For a fixed frequency component and $K=500$, the optimal sampling frequency is highly influenced by the damping factor. As the damping factor increases, the optimal sampling frequency also increases. The estimate variance also increases with the increase in damping factor. MPM is unable to estimate well for highly damped signals. One possible reason for this is that with a high damping factor, the signal is quickly attenuated and much lesser useful information can be processed by MPM.
- As the results are shown in discrete parameters, they can be applied to a general set of sampled complex damped exponential signals with appropriate mathematical manipulation.

3.3.5 Acknowledgments

The graphs in this chapter have been plotted with the use of Python 2.7.3 release [44] using EPD Free [45] with the following packages:

- Matplotlib [46]
- SciPy [47] and
- Numpy [48]

Chapter 4

Performance of MPM: Amplitude and Phase Estimation

This chapter examines the performance of MPM on extracting the amplitude and phase information. Similar to the Chapter 3, a statistical analysis of the feature extraction capability of MPM has been carried out on the test signal as described in Subsection 3.2.2.

4.1 Effects of Varying Sampling Frequency and Sampling Window Width

In this section, the effect of changing the sampling frequency and sampling window width on the estimation of amplitude and phase is examined. The sampling period, T_s , was varied between 0.01 s and 1 μ s while sampling window width, K , was varied between 10 and 500.

4.1.1 Amplitude and Phase Estimation

The amplitude estimate mean error and variance are shown in Figure 4.1. The discrete angular frequency, ω_N , is plotted against K ($\omega_N = \omega T_s$). It can be observed from Figure 4.1a and b, as ω_N becomes closer to the Nyquist frequency ($\omega_N = \pi \approx 10^{0.5}$), both the estimate error and variance increase. On the other hand, the variance of the estimate reduces for small ω_N and large K . This means that the amplitude can be best estimated when sampling window width, K is large and the sampling period, T_s is small.

The phase estimation results are shown in Figure 4.2. The phase estimation performance is very similar to that of the amplitude estimation performance in that the phase is also best estimated when sampling window width, K is large and sampling period, T_s is small.

In comparison, the accuracy of DFT's estimates of amplitude and phase of the signal depends on how closely the signal's frequency matches that of the frequency bins. If the signal frequency lies somewhere in between two frequency bins, then the signal will be leaked into the surrounding frequency bins, resulting in inaccurate answers. Increasing K increases the DFT's frequency resolution and reduces leakage. Hence, this also improves the accuracy of amplitude and phase estimation of DFT.

4.2 Effects of Varying the Frequency Component and Sampling Period

In this section, the amplitude and phase estimation performances have been assessed by varying the angular frequency, ω , and sampling period, T_s while keeping the other parameters constant. The objective is to assess

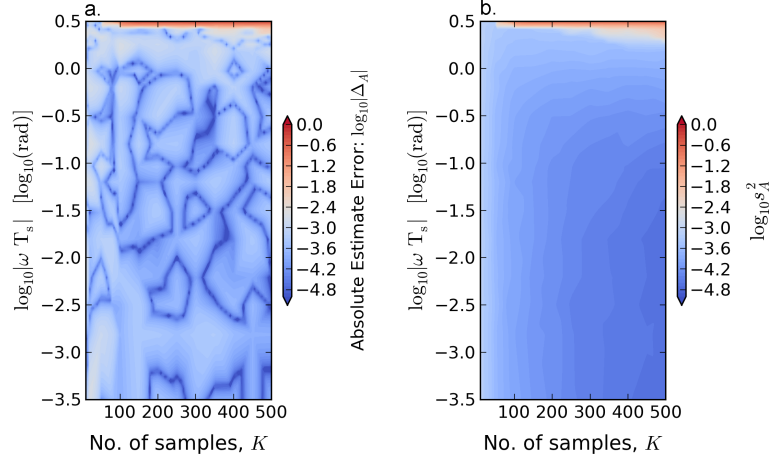


Figure 4.1: a. Mean Absolute Estimate Error and b. Variance of Amplitude Estimate for different T_s and K on Signal, $1.0e^{(j\frac{10}{180}\pi)}e^{[-5.0+j2\pi(50)]t}$

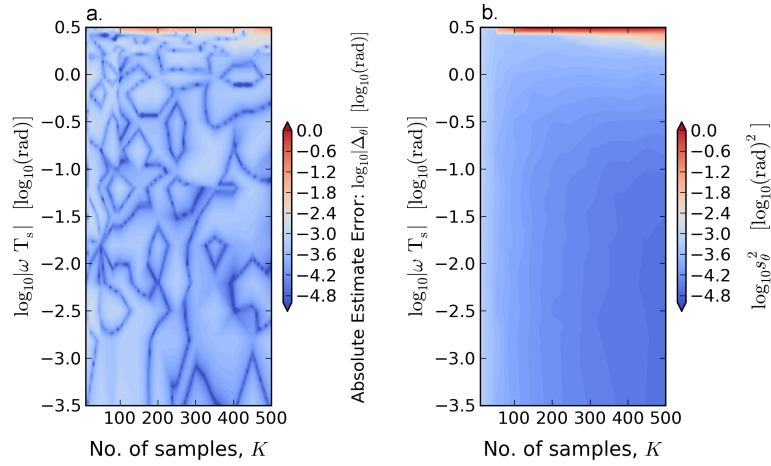


Figure 4.2: a. Mean Absolute Estimate Error and b. Variance of Phase Angle Estimate for different T_s and K on Signal, $1.0e^{(j\frac{10}{180}\pi)}e^{[-5.0+j2\pi(50)]t}$

the effect of varying the frequency, ω , on the optimal sampling frequency.

The sampling window width, K , was set at a constant of 500, and the damping factor, α was set at a constant of -5.0 s^{-1} . The frequency component was swept from 0.01 Hz to 3000 Hz and the sampling period was varied from $1 \mu\text{s}$ to 0.01 s.

4.2.1 Amplitude and Phase Estimation

As shown in Figure 4.3 and 4.4, the estimation performance of amplitude and phase stays similar for the same α_N . Similar to damping and frequency estimates, the frequency component changes did not have a large effect on the estimation performance. The variances reduce as the sampling period, T_s , becomes shorter.

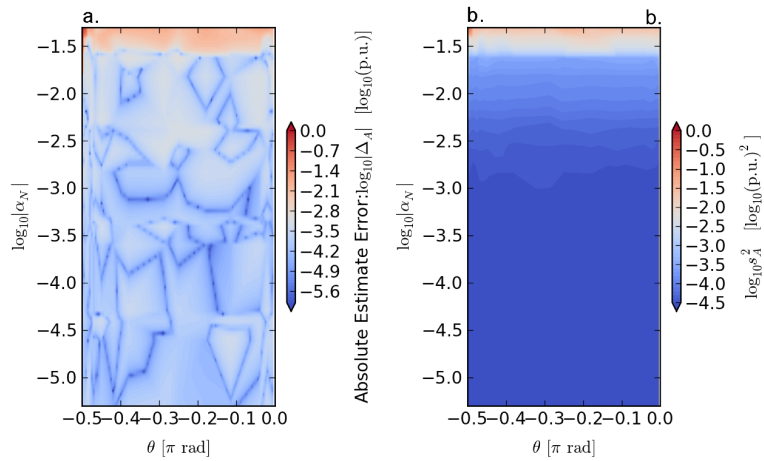


Figure 4.3: a. Mean Absolute Estimate Error and b. Variance of Amplitude Estimate for different sampling period, T_s and complex exponential angle, θ . Sampling Window Width, $K = 500$, and Damping Factor, $\alpha = -5.0\text{s}^{-1}$.

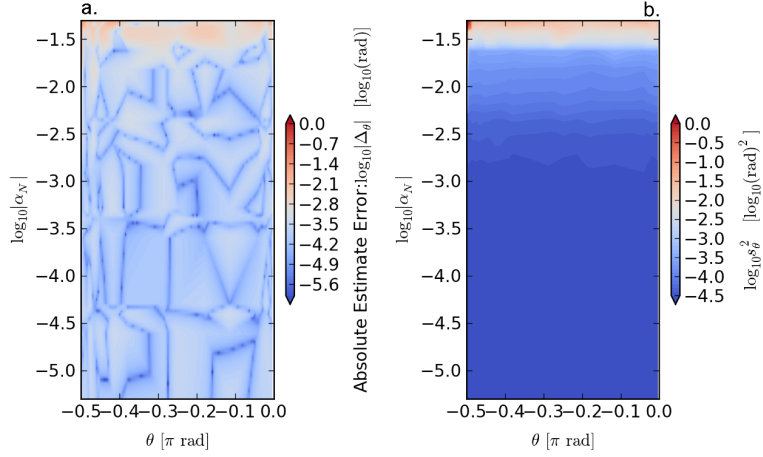


Figure 4.4: a. Mean Absolute Estimate Error and b. Variance of Phase Estimate for different sampling period, T_s and complex exponential angle, θ . Sampling Window Width, $K = 500$, and Damping Factor, $\alpha = -5.0s^{-1}$.

4.2.2 Comparison with Damping Factor and Frequency Estimates

The damping factor and frequency estimate variances are put together with those of amplitude and phase estimates for comparison in Figure 4.5. The amplitude and phase estimate variances reduce as the sampling period decreases. This is different from the damping factor and frequency component estimation where the variances are the lowest when $\alpha_N = -10^{-2.4}$. The variances deteriorate even as the sampling period reduces thereafter.

4.3 Effects of Damping Factor Variation and Sampling Frequency

In this last section, the damping factor and sampling period, T_s , are varied while keeping K at 500 and frequency component at 50 Hz. The objective is to assess the effect of varying the damping factor, α , on the

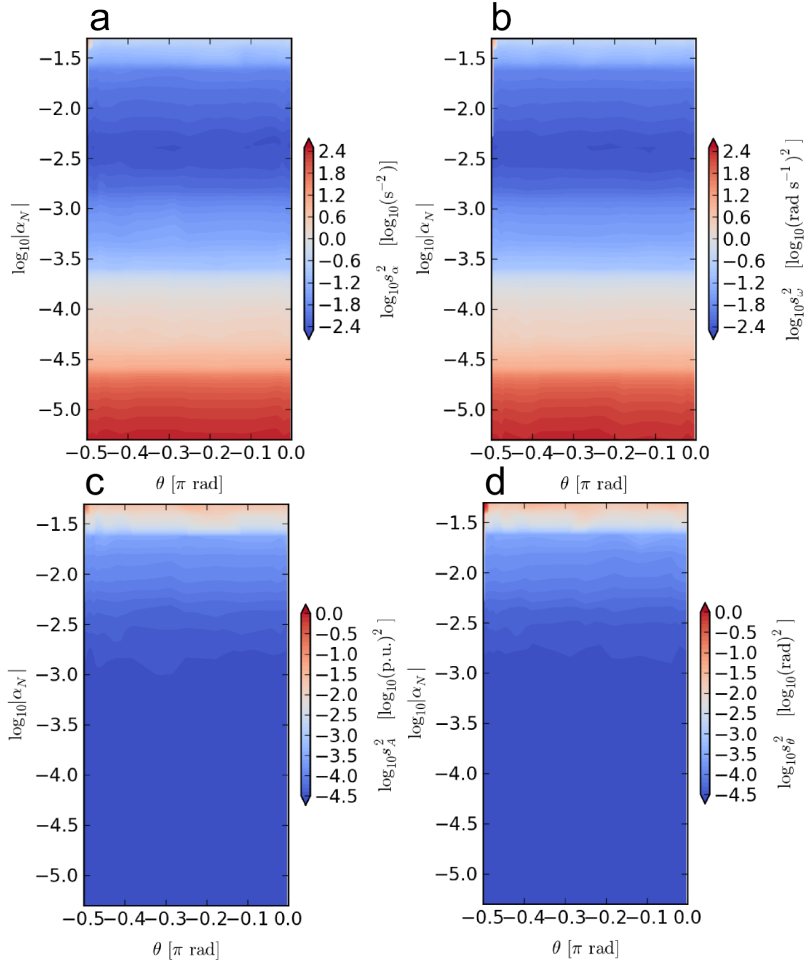


Figure 4.5: Variance Estimates of a. Damping Factor, b. Frequency, c. Amplitude and d. Phase Angle Estimate for different sampling period, T_s and complex exponential angle, θ . Sampling Window Width, $K = 500$, and Damping Factor, $\alpha = -5.0\text{s}^{-1}$.

optimal sampling frequency. The damping factor was swept from -0.01 s^{-1} to $-50,000 \text{ s}^{-1}$ while the sampling period was varied from $1 \mu\text{s}$ to 0.01 s .

4.3.1 Amplitude and Phase Estimation

The results for amplitude and phase estimates are shown in Figure 4.6 and 4.7. The amplitude and phase estimate variances reduce as sampling period, T_s , decreases. This means that high sampling frequency can im-

prove amplitude and phase estimation.

In addition, when the signal is lightly damped (ie when $\theta \approx -0.5\pi$ rad), both amplitude and phase can be well estimated at around $\omega_N \approx 10^{-0.5}$ rad. However, as the damping factor increases, ω_N has to reduce in order to get a good amplitude estimate. This means that a higher sampling frequency is needed for highly damped signals. For example, using a undamped 50 Hz signal with sampling window width of $K=500$ as an example, a sampling frequency of about 1 kHz can achieve a approximate amplitude estimate variance of $10^{-4} s^{-2}$, whereas a sampling frequency of 100 kHz is needed for a damped 50 Hz signal of $\alpha = -105 s^{-1}$ for a similar estimate variance.

A discrepancy is observed in Figure 4.6b, where the amplitude estimate variance is unexpectedly low in the circled blue region. It was because MPM was estimating the amplitude with a consistent error. This can be observed in Figure 4.6a where the absolute error was large in the same region.

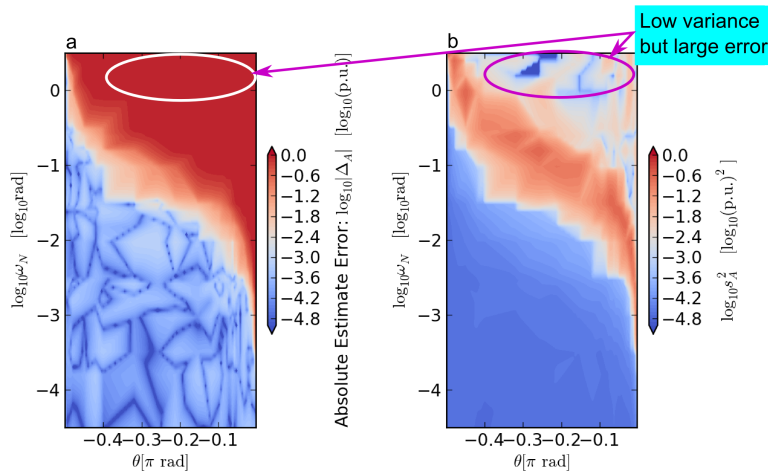


Figure 4.6: a. Mean Absolute Estimate Error and b. Variance of Amplitude Estimate for different sampling period, T_s and complex exponential angle, θ . Sampling Window Width, $K = 500$, and Frequency, $\omega = 2\pi(50.0)\text{rad s}^{-1}$.

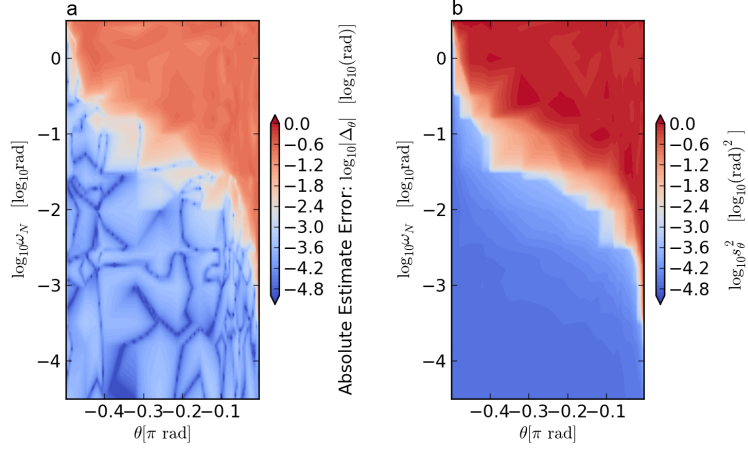


Figure 4.7: a. Mean Absolute Estimate Error and b. Variance of Phase Estimate for different sampling period, T_s and complex exponential angle, θ . Sampling Window Width, $K = 500$, and Frequency, $\omega = 2\pi(50.0)\text{rad s}^{-1}$.

4.3.2 Comparison with Damping Factor and Frequency Estimates

Figure 4.8 shows the estimate variances for all the four parameters that MPM extracts. All four estimates are highly influenced by the damping factor variations. When the signal is lightly damped (ie $\theta \approx -0.5\pi$ rad), all four can be estimated well with a relatively large sampling period of $\omega_N \approx 10^{-0.5}$ rad. However, as the signal becomes heavily damped, the sampling period, T_s , has to be reduced for an accurate estimate.

The amplitude and phase estimates have a different behavior than those of damping factor and frequency estimates. The amplitude and phase estimations improve consistently as the sampling period decreases while the frequency and damping factor estimates do not. The frequency and damping factor can only be well estimated within a small region close to $\theta \approx -0.5\pi$ rad and bounded by ω_N between $10^{0.2}$ and 10^{-3} rad.

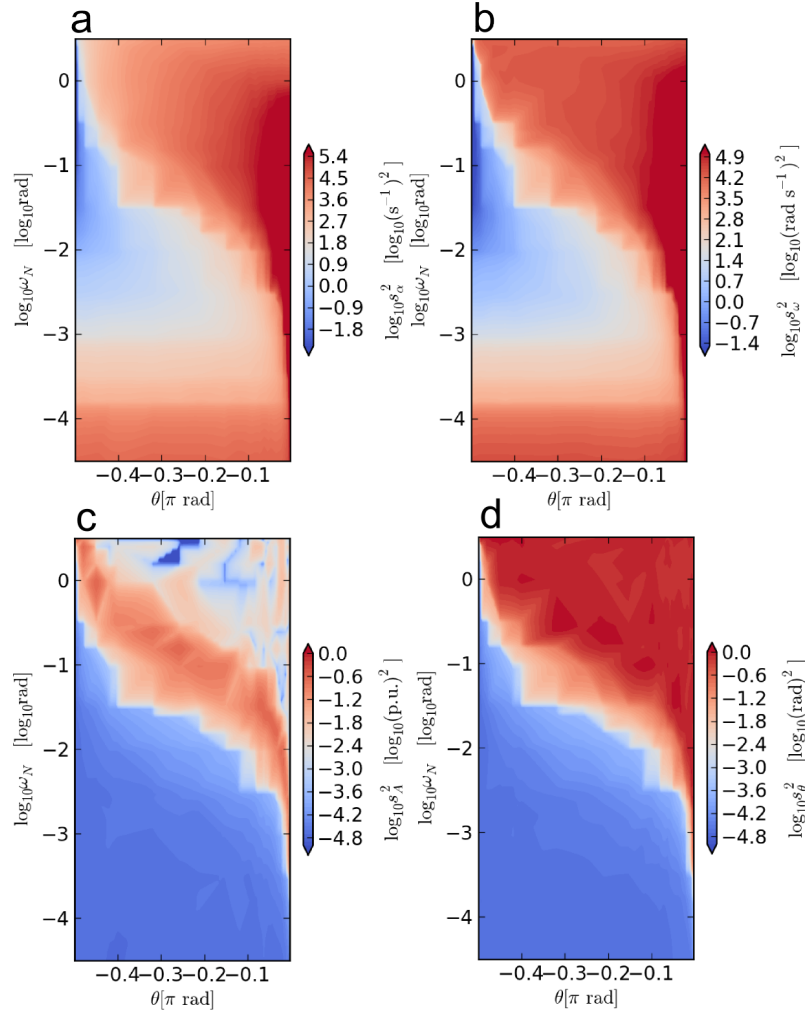


Figure 4.8: Variance Estimates of a. Damping Factor, b. Frequency, c. Amplitude and d. Phase Angle Estimate for different sampling period, T_s and complex exponential angle, θ . Sampling Window Width, $K = 500$, and Frequency, $\omega = 2\pi(50.0)\text{rad s}^{-1}$.

4.4 Summary

In summary, the following are the useful pointers following the statistical analysis of the parameter estimates.

- In general, the amplitude and phase estimate variances reduce as the number of samples, K , increases. In comparison, the accuracy

of DFT's estimates are generally affected by leakage. Increasing K increases the DFT's frequency resolution, reduces leakage and hence improves the accuracy of amplitude and phase estimation of DFT.

- The amplitude and phase estimates also perform better at higher sampling frequencies for a fixed sampling window width, K . This is different from damping factor and frequency component estimates where the variances deteriorate after the sampling frequency increases beyond the optimal sampling frequency.
- For a given damping factor and $K=500$, the estimate variances depend largely on the sampling frequency. Varying the frequency component did not affect the variance much.
- For a given frequency component and $K=500$, the amplitude and phase estimates perform well when the damping factor is small. Generally, these estimates improve as the sampling period decreases. Hence, the sampling period has to be reduced for good performance when the damping factor increases. As an interesting comparison, this is different from the damping factor and frequency component estimates where they are well estimated only within a small region where damping factor is small and ω_N is approximately between $10^{0.2}$ and 10^{-3} rad.

One possible reason for better performance at high sampling frequency and large K is that the amplitude of the signal is the largest at the start as the signal is damped. Hence, a high sampling frequency and a large K will capture the most information about the amplitude and phase of the signal and hence result in a better estimation.

Chapter 5

Application of MPM on Subcycle Voltage Dip and Swell Classification

5.1 Introduction

Voltage dips and swells are an important class of Power Quality (PQ) disturbances and are often caused by faults in the power network. They can cause large economic losses in industrial systems [49], [50] especially with the increased use of sensitive power electronics devices in industry. About 10 to 15% of faults exhibit incipient half-cycle self-clearing fault events for anywhere between two cycles to two weeks before developing into a full-blown permanent fault [51]. The analysis of such sub-cycle faults thus presents us with an opportunity to rectify the imminent fault before it causes a disastrous fault event. The classification of voltage dips is certainly a first step towards the analysis of such sub-cycle faults.

As the penetration rate of Distributed Energy Resource (DER)'s increases, there is a need to perform faster analysis on electrical phenomena

especially for fault conditions. Most of these DER's are connected at the distribution level via sensitive power electronic converters and these converters would disconnect in less than 50 ms or 2.5-cycle time when voltage sags to below 50% of the nominal value [52]. Sub-cycle analysis of faults or other grid events can provide timely information for the devices to react quickly.

There is also a trend towards increased intelligence at the distribution level [53]. Distribution networks have traditionally been designed for uni-directional power flow from transmission networks to the loads on the distribution levels. However, with more active components such as DER's and batteries connected at distribution level, intelligence is needed to monitor, analyze and control various operations such as bi-directional power flows, voltage regulation, fault protection etc. at the distribution level. Sub-cycle analysis of faults or other grid events can enable the intelligent device to do that.

At the onset of the fault occurrence, the voltage signal will exhibit a transient behaviour before settling down to a steady state fundamental frequency sinusoidal fault signal. This steady-state fault signal depends on the type of fault and is often analyzed using Fortescue's [54] symmetrical components. Most conventional fault analysis algorithms [55, 1, 56] rely on the phasor information of at least 1 cycle of the steady state fault signal. In many cases however, faults occur in an intermittent fashion before a permanent fault occurs [57, 51]. One such example is underground cable fault [51, 58]. They cause voltage disturbances to last only for less than two or even one cycle before reverting to normal voltage signals. These intermittent faults may have cleared within the cycle, and thus conventional algorithms do not suffice to provide a good analysis of such faults. A sub-cycle analysis method is required.

Intermittent faults are also often precursors to permanent faults to come. Hence, a proper analysis of them can glean important information to rectify possible equipment failure to prevent imminent permanent faults and unforeseen service outages. Such analysis can be executed offline on recorded signals to provide a diagnosis of the situation.

Fault analysis methods often rely on mathematical transformation of the three-phase quantities into orthogonal components. Conventionally, the use of symmetrical components [54] is the most common method of fault analysis. Vanya [1] on the other hand, developed an algorithm based on Clarke [59] transformation to classify the voltage dip signatures into the major fault types. Clarke transformation is suitable for subcycle analysis as it deals with instantaneous quantities instead of phasor quantities.

As the electrical signals usually consist of a fundamental 50 Hz component together with transient, harmonics, sub-harmonic and inter-harmonic components, the signals have to be processed beforehand to extract the useful components. The comparisons of various signal processing techniques have been explained in detail in Chapter 1 and shall quickly mentioned here for completeness. FFT is the most common signal processing technique employed to analyze electrical signals. However, FFT suffers from problems such as an inability to extract damping information and the frequency resolution limited by the sampling window width. Another well-known signal processing technique, Prony analysis [30] estimates similar components as MPM, but they differ in the way the signal poles are extracted. MPM has been shown to perform better in noise and has fewer limitations in comparison [32, 33]. Furthermore, the Prony analysis sampling window length has to be at least one and a half times the period of frequency of interest [34] and cannot be used for sub-cycle analysis. Based on the findings in Chapter 3 and 4, MPM shall be further examined in this chapter to show

that it is able to provide a relatively good estimate of the signal parameters with only a sub-cycle sampling window or in other words, less than 20 ms window for a 50 Hz signal.

In this chapter, the three-phase voltage signals are transformed via Clarke transformation [59] to form a space vector using the resulting α and β components. This space vector is then processed using the MPM method to elucidate the fundamental positive- and negative-sequence components. The zero-sequence signal is also processed with MPM to extract the fundamental frequency amplitude and phase information. These information are then used to classify the voltage dip using the criteria proposed by Vanya [1]. The reader should note that this thesis limits the discussion to the use of MPM on the classification of voltage dips and swells after fault detection and segmentation. Fault detection is the process in which the start or end points of the fault are located while segmentation is the process in which portions of the voltage signal is divided into pre-fault, on-fault and post-fault segments. There are already several techniques of fast fault detection and segmentation in literature based on high frequency content of the signals at the start and end of faults [60, 61] or based on changes in voltage magnitudes [62]. These methods can be used to detect and segment the signals before the application of fault classification. They are however not included in the scope of this thesis.

Two similar and distorted fault signals were created by simulating a two-phase fault and two-phase-to-ground fault signals. These faults were created in a simple case test system and also in an IEEE 34-bus system to test the efficacy of the method. The results show that MPM is able to estimate the fundamental frequency space vector components effectively with a 5 ms sampling window in the simple test case. An ellipse fitting algorithm is augmented to the MPM to enhance the estimation performance

in highly distorted signals in the IEEE 34-bus system. As an example, it differentiated between two highly similar faults with a 5 ms sampling window, demonstrating the feasibility of this scheme. A further improvement was made to the method by filtering and downsampling the signals before processing it with MPM. This reduced the computation time of the algorithm to 3 ms. In total, the improved algorithm can classify the dip within 9 ms to 10 ms from the onset of the fault. This is an improvement over the Vanya's [1] method of using DFT that required at least a 20-ms sampling window.

5.2 Classification of Voltage Dips and Swells using Space Vector [1]

It is well known that a complex space vector, \vec{v} , can be formed with the following equation using the α and β components via Clarke Transform [59]:

$$\vec{v} = \frac{2}{3}[v_a(t) + e^{j(2\pi/3)}v_b(t) + e^{-j(2\pi/3)}v_c(t)] = v_\alpha(t) + jv_\beta(t) \quad (5.1)$$

Space vectors are suited for the analysis of instantaneous voltages and currents [59], [63]. However, as a simplification for a three-phase set of unbalanced, distorted periodic phase voltages containing only harmonic components, the space vector may be represented in Equation (5.2) as derived by Zhang [64].

$$\vec{v} = \sum_{n=1}^{\infty} V_{n+} e^{j\phi_{n+}} \cdot e^{j(n\omega t)} + \sum_{n=1}^{\infty} V_{n-} e^{j\phi_{n-}} \cdot e^{-j(n\omega t)} \quad (5.2)$$

where ω is the fundamental angular frequency and n represents the harmonic order of the component. $V_{n+}e^{j\phi_{n+}}$ and $V_{n-}e^{j\phi_{n-}}$ represents the n^{th} harmonic Fortescue's [54] positive sequence and negative sequence phasor

components respectively. The fundamental frequency space vector component, v_1 , can thus be expressed in Equation (5.3) as the sum of two phasors contra rotating at fundamental frequency.

$$\vec{v}_1 = V_{1+}e^{j\phi_{1+}} \cdot e^{j(\omega t)} + V_{1-}e^{j\phi_{1-}} \cdot e^{-j(\omega t)} \quad (5.3)$$

During unbalanced faults, these contra rotating phasors with different amplitudes and phases add together to form an ellipse. The major axis, r_{maj} , minor axis, r_{min} , inclination angle, ϕ_{inc} , and shape index, SI can then be calculated [1]. They are defined as follows:

$$\begin{aligned} r_{maj} &= V_{1+} + V_{1-} \\ r_{min} &= |V_{1+} - V_{1-}| \\ \phi_{inc} &= 0.5(\phi_{1+} + \phi_{1-}) \\ SI &= \frac{r_{min}}{r_{maj}} \end{aligned} \quad (5.4)$$

The zero-sequence voltage is defined as:

$$v_0(t) = \frac{1}{3}[v_a(t) + v_b(t) + v_c(t)] \quad (5.5)$$

Similar to Equation 5.2, the zero-sequence voltage can be simplified into a sum of harmonic components as:

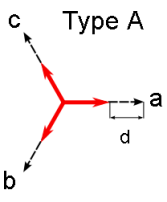
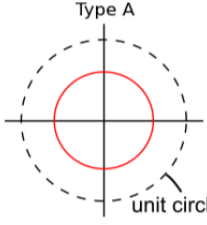
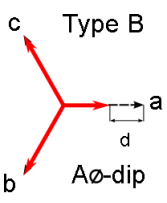
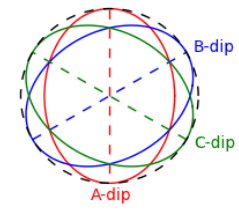
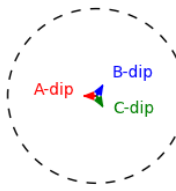
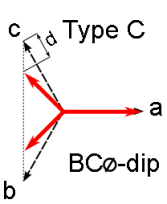
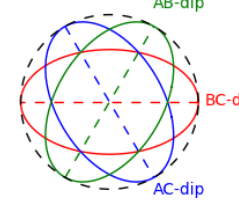
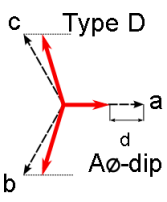
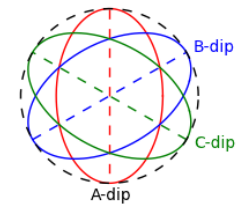
$$v_0(t) = \sum_{n=1}^{\infty} V_{n0} \cos(n\omega t + \phi_{n0}) \quad (5.6)$$

The fundamental frequency zero-sequence component can thus be defined as:

$$v_{10}(t) = V_{10} \cos(\omega t + \phi_{10}) \quad (5.7)$$

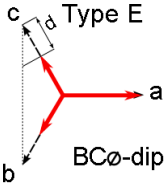
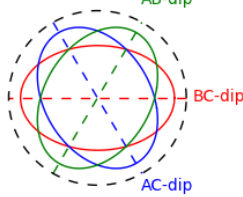
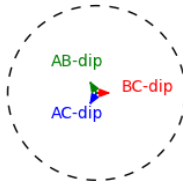
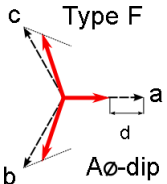
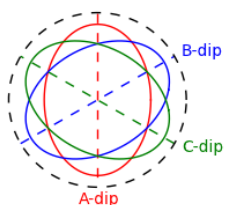
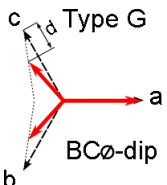
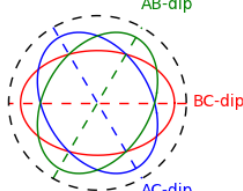
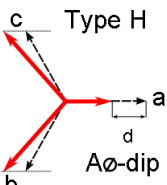
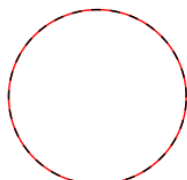
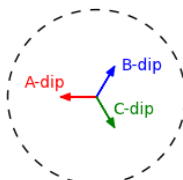
These metrics can then be used to classify ten different dip types. These types are extracted from [4, 1] and are shown in Table 5.1. Their corresponding metrics are tabulated in Table 5.2. Note that Type I* and I** are closely related and are thus labeled as such in [1].

Table 5.1: Dip Types' Voltage Phasors and Space Vectors (Adapted from [4, 1])

Voltage Phasors	Space-vectors	V_{10} Phasors
 <p>Type A</p>	 <p>Type A</p> <p>unit circle</p>	$V_{10} = 0$
 <p>Type B</p> <p>AØ-dip</p>	 <p>Type B</p> <p>B-dip</p> <p>C-dip</p> <p>A-dip</p>	 <p>Type B</p> <p>A-dip</p> <p>B-dip</p> <p>C-dip</p>
 <p>Type C</p> <p>BCØ-dip</p>	 <p>Type C</p> <p>AB-dip</p> <p>BC-dip</p> <p>AC-dip</p>	$V_{10} = 0$
 <p>Type D</p> <p>AØ-dip</p>	 <p>Type D</p> <p>B-dip</p> <p>C-dip</p> <p>A-dip</p>	$V_{10} = 0$

Continued on next page

Table 5.1 – continued from previous page

Voltage Phasors	Space-vectors	V_{10} Phasors
 <p>Type E BCØ-dip</p>	 <p>Type E AB-dip BC-dip AC-dip</p>	 <p>Type E AB-dip BC-dip AC-dip</p>
 <p>Type F AØ-dip</p>	 <p>Type F B-dip C-dip A-dip</p>	<p>$V_{10} = 0$</p>
 <p>Type G BCØ-dip</p>	 <p>Type G AB-dip BC-dip AC-dip</p>	<p>$V_{10} = 0$</p>
 <p>Type H AØ-dip</p>	 <p>Type H</p>	 <p>Type H A-dip B-dip C-dip</p>

Continued on next page

Table 5.1 – continued from previous page

Voltage Phasors	Space-vectors	V_{10} Phasors
<p>Diagram showing three voltage phasors labeled 'a', 'b', and 'c' originating from a common point. Phasor 'a' is horizontal to the right. Phasors 'b' and 'c' are at approximately 120 degrees and 240 degrees respectively. A dashed line 'd' is shown perpendicular to 'a'. The label 'Type I*' is at the top, and 'BCØ-dip' is at the bottom.</p>	<p>A circle with a red dashed line and a solid black line, representing the space vector locus for Type I*.</p>	<p>A dashed circle containing three phasors: 'AB-dip' (green), 'BC-dip' (red), and 'AC-dip' (blue). The phasors are arranged in a Y-shape.</p>
<p>Diagram showing three voltage phasors labeled 'a', 'b', and 'c' originating from a common point. Phasor 'a' is horizontal to the right. Phasors 'b' and 'c' are at approximately 120 degrees and 240 degrees respectively. A dashed line 'd' is shown perpendicular to 'a'. The label 'Type I**' is at the top, and 'BCØ-dip' is at the bottom.</p>	<p>A 3D representation of a sphere with three intersecting loops (green, red, blue) representing the space vector locus for Type I**. The loops are labeled 'AB-dip', 'BC-dip', and 'AC-dip'.</p>	<p>A dashed circle containing three phasors: 'AB-dip' (green), 'BC-dip' (red), and 'AC-dip' (blue). The phasors are arranged in a Y-shape.</p>

5.3 Application of MPM

5.3.1 Signals of interest

MPM is employed to estimate the fundamental frequency space vector component previously expressed in Equation 5.3. In order to extract the information, a sliding window of 500 samples of the three phase voltages were transformed into $\alpha - \beta - 0$ components. The $\alpha - \beta$ components form the space vector and is processed by MPM directly to estimate the complex exponential components. Thereafter, to examine only the fundamental ± 50 Hz components, the two components closest to 50Hz and -50Hz respectively are extracted for evaluation. We then form the estimated fundamental frequency space vector as expressed in Equation 5.3.

Table 5.2: Classification of Voltage Dip and Swells based on Space Vector and Zero-Sequence Voltage [1]

Dips	Type	Space Vector				Zero Sequence Voltage
		SI	ϕ_{inc}	r_{min}	r_{maj}	
1-ϕ Dips	B	$1 - \frac{2}{3}d$	$\frac{5\pi}{6} - n_f \frac{\pi}{3}$	$(1 - \frac{2}{3}d)V$	V	$-\frac{d}{3}V \cos(\omega t + \phi - (n_f - 1)\frac{2\pi}{3})$
	D	$1 - d$	$\frac{5\pi}{6} - n_f \frac{\pi}{3}$	$(1 - d)V$	V	0
	F	$\frac{3(1-d)}{3-d}$	$\frac{5\pi}{6} - n_f \frac{\pi}{3}$	$(1 - d)V$	$(1 - \frac{d}{3})V$	0
2-ϕ Dips	C	$1 - \frac{4}{3}d$	$(1 - n_{nf})\frac{\pi}{3}$	$(1 - \frac{4}{3}d)V$	V	0
	E	$\frac{3(1-d)}{3-d}$	$(1 - n_{nf})\frac{\pi}{3}$	$(1 - d)V$	$(1 - \frac{d}{3})V$	$\frac{d}{3}V \cos(\omega t + \phi - (n_{nf} - 1)\frac{2\pi}{3})$
	G	$\frac{5-6d}{5-2d}$	$(1 - n_{nf})\frac{\pi}{3}$	$(1 - \frac{6}{5}d)V$	$(1 - \frac{2d}{5})V$	0
3-ϕ Dips	A	1	-	$(1 - d)V$	$(1 - d)V$	0
Dip with Rise in non-faulted Phases	H	1	-	V	V	$-dV \cos(\omega t + \phi - (n_f - 1)\frac{2\pi}{3})$
	I*	1	-	V	V	$2dV \cos(\omega t + \phi - (n_{nf} - 1)\frac{2\pi}{3})$
	I**	$\frac{4}{3}(1 - d)$	$(1 - n_{nf})\frac{\pi}{3}$	$\frac{4}{3}(1 - d)V$	V	$\frac{V}{2} \cos(\omega t + \phi - (n_{nf} - 1)\frac{2\pi}{3})$

n_f = Faulted phase with dip.

n_{nf} = Non-faulted Phase with no dip. $n_{nf}, n_f = 1, 2, 3$ for phase A, B and C respectively.

ϕ = Positive Sequence Phase Angle.

$V = 1.0$ p.u.

d = Dip depth.

The 0-component is also processed separately by MPM to extract the 50 Hz component. As it is a real signal, it contains both the positive and negative frequency component with the same information. Hence, only one of them (the positive frequency component) was extracted for post processing. With these information, the metrics in Equation 5.4 can be calculated to classify the voltage dip.

5.4 Choice of Sampling Frequency

Our objective is to analyze and classify the fault within the shortest possible time. Hence, it is important to know how the feature extraction performance of MPM is affected with shorter time sampling window. From Chapter 3 and 4, the feature extraction performance of MPM has been analyzed for a range of discrete angular frequency, ω_N by varying damping factors and sampling frequencies. In this section, with the same information, we have calculated the number of cycles of the analog test signal, $1.0e^{(j\frac{10}{180}\pi)}e^{[\alpha+j2\pi(50)]t}$ described in Subsection 3.2.2. The calculation was done with $K = 500$ samples and the discrete angular frequency ω_N using Equation 5.8.

$$\text{Number of Cycles} = K \times \frac{\omega_N}{2\pi} \quad (5.8)$$

Figure 5.1 shows the various estimate variances in relation to the complex exponential angle, θ and number of cycles of the analog signal in the sampling window. In this way, the feature extraction performance can be estimated for different sampling window widths in terms of number of sinusoidal cycles.

In Figure 5.1b, a region where the angular frequency variance, s_ω^2 is less than $(2\pi)^2(\text{rads}^{-1})^2$ is marked out by the dashed line. Taking the square root of the variance, the angular frequency standard deviation, s_ω ,

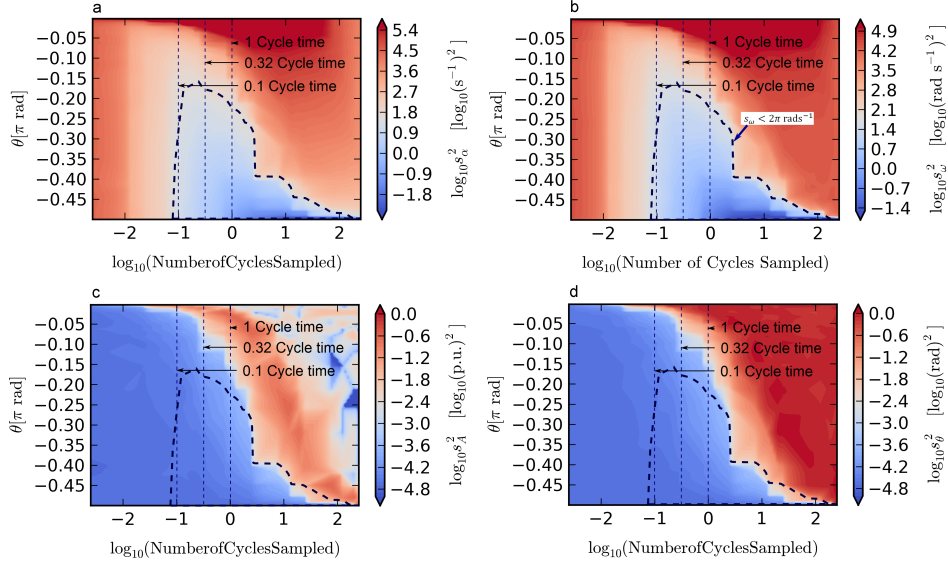


Figure 5.1: Variance of a. Analog Angular Frequency, b. Analog Damping Factor, c. Amplitude, d. Phase Angle Estimates of Signal, $Ae^{j\frac{10}{180}\pi}e^{[\frac{2\pi(50)}{\tan\theta} + j2\pi(50)]t}$

is thus less than $2\pi(\text{rads}^{-1})$. This is equivalent to the frequency standard deviation, s_f , less than 1 Hz. In reference to power system context, the frequency range for a generator to operate indefinitely without disconnecting from the grid is ± 1 Hz from the nominal frequency of 50 Hz according to the European Network of Transmission System Operators for Electricity (ENTSO-E) proposed harmonized grid code [65].

In this region, we can observe that for a signal with complex exponential angle, $\theta < -0.20\pi$ rad or equivalently, a damping factor of less than -593.6 s^{-1} for a 50 Hz signal, the signal frequency can be estimated within a variance of 1 Hz^2 . In addition, this can be achieved with 0.1 to 1 cycle of the signal.

The same region is marked out on the other variance plots. The damping factor estimate standard deviation, s_α , is less than $\sqrt{10^{1.8}} \approx 8 \text{ s}^{-1}$ in the same region. For the amplitude and phase angle estimates, the variances

reduce with lesser number of cycles and lower damping factors. They are well estimated with 0.1 to 1 cycles of samples.

All in all, these figures show that MPM can provide a fairly good parameter estimates of a moderately damped complex exponential signal of $\theta < -0.20\pi$ rad with 0.1 to 1 cycle of the signal.

A subcycle sample window of 5 ms which is 0.25 times of a 50 Hz signal cycle has been chosen instead of 0.1 cycle for our use so as to better estimate signals with higher damping factors. With 500 samples, the sampling frequency is calculated to be 100 kHz.

5.4.1 Signal Processing and Classification Algorithm

The fundamental frequency space vectors are first estimated by MPM to derive the ellipse parameters listed in Equation 5.4. The first step is to categorize the dip into two groups. For $1-\phi$, $2-\phi$ and I^{**} dip types, the value of SI depends on the dip depth, d , while for the rest of the dip types, $SI=1$. They are hereby named Group 1 and Group 2 dip types respectively. IEEE 1346-1998 standard [66] defined a sag to be a decrease in Root-Mean-Squared (RMS) voltage with typical values of 0.1 to 0.9 pu. Group 1 dip types will thus have SI of less than 0.933 with a minimum dip depth, d of 0.1 pu. Hence, voltage dips with $SI < 0.933$ are classified under Group 1 dip types while those with $SI \geq 0.933$ are classified as Group 2 dip types.

The Group 1 dip types can be further differentiated by comparing the inclination angle, ϕ_{inc} , the major axis, r_{maj} and the fundamental frequency zero-sequence voltage magnitude, $|V_{10}|$ as shown in Table 5.3. The ϕ_{inc} determines affected phase(s). The single phase dip types are B, D and F and the two phase dip types are E, C, G and I^{**} . $|V_{10}|$ and r_{maj} then further differentiate among these various dip types. The threshold values

for $|V_{10}|$ and r_{maj} in Table 5.3 are calculated by substituting the minimum dip depth, $d = 0.1$ pu, into their respective equations in Table 5.2. In order to reduce computational resources, MPM is used to extract the V_{10} component only when the magnitude of any of the zero-sequence voltage samples in the sampling window is larger than 0.03 pu. Otherwise, $|V_{10}|$ will be taken as 0.0 pu.

Group 2 dips consist of only Types A, H and I*. They can be further classified by evaluating the zero-sequence voltage magnitude and phase as shown in Table 5.4. $|V_{10}|$ is at least 0.1 pu for Type H and I* dips for a minimum d of 0.1 pu, while $|V_{10}|$ is zero for Type A. Then the phase difference between fundamental frequency zero-sequence and positive sequence component is used to differentiate between H and I* dips.

5.4.2 Simulation of fault and Discussion

Simulation Setup - Simple Theoretical Case

A simple theoretical case is first built in PowerFactory [67] to test the classification algorithm. This is shown in Figure 5.2. A 20 kV three-phase voltage source is connected to a typical Dy transformer and then connected to a 2 km cable with capacitance modeled in. A Type E dip was generated with a two-phase-to-ground fault [4] at the 1km point on the cable. The fault three-phase voltage waveforms are shown in Figure 5.3. The distortions are caused by the interactions between the capacitance and reactances in the system.

Estimation of the Shape Index, SI , $|V_{10}|$, ϕ_{inc} and r_{maj}

In the first step of the classification algorithm, the SI has to be estimated to categorize the faults into either Group 1 or Group 2 dip types.

Table 5.3: Group I Classification

ϕ_{inc}	$ V_{10} $	r_{maj}	Dip Types	Phase(s) Dip
$90 \pm 15^\circ$	≥ 0.033 pu	≥ 0.967 pu	B	$A\phi$
	< 0.033 pu	≥ 0.967 pu	D	
	< 0.033 pu	< 0.967 pu	F	
$30 \pm 15^\circ$	≥ 0.033 pu	≥ 0.967 pu	B	$B\phi$
	< 0.033 pu	≥ 0.967 pu	D	
	< 0.033 pu	< 0.967 pu	F	
$-30 \pm 15^\circ$	≥ 0.033 pu	≥ 0.967 pu	B	$C\phi$
	< 0.033 pu	≥ 0.967 pu	D	
	< 0.033 pu	< 0.967 pu	F	
$0 \pm 15^\circ$	≥ 0.033 pu	< 0.967 pu	E	$B\phi$ and $C\phi$
	≥ 0.033 pu	≥ 0.967 pu	I**	
	< 0.033 pu	≥ 0.960 pu	C	
	< 0.033 pu	< 0.960 pu	G	
$-60 \pm 15^\circ$	≥ 0.033 pu	< 0.967 pu	E	$A\phi$ and $C\phi$
	≥ 0.033 pu	≥ 0.967 pu	I**	
	< 0.033 pu	≥ 0.960 pu	C	
	< 0.033 pu	< 0.960 pu	G	
$-120 \pm 15^\circ$	≥ 0.033 pu	< 0.967 pu	E	$A\phi$ and $B\phi$
	≥ 0.033 pu	≥ 0.967 pu	I**	
	< 0.033 pu	≥ 0.960 pu	C	
	< 0.033 pu	< 0.960 pu	G	

Table 5.4: Group 2 Classification based on $|V_{10}|$ and $\phi_{10} - \phi_{1+}$

Dip Type	$ V_{10} $	$\phi_{10} - \phi_{1+}$
A	< 0.1 pu	N.A.
H	≥ 0.1 pu	$-(n_f - 1) \times (120^\circ) + 180^\circ$
I*	≥ 0.1 pu	$-(n_{nf} - 1) \times (120^\circ)$

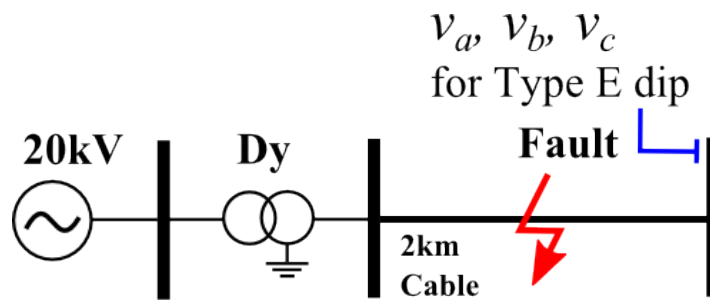


Figure 5.2: Single Line Diagram of Simple Theoretical Case

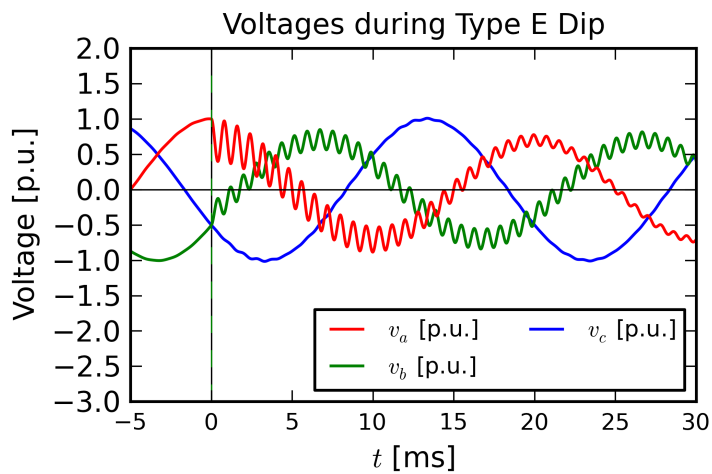


Figure 5.3: Fault waveforms generated for simple case

The results are shown in Figure 5.4. The time, t , represents the time stamp of the last sample in the sampling window. The fault occurred at $t = 0.0$ s. The region between 0 and 5 ms are coloured in grey as the sampling window straddles across pre-fault and faulted regions. Straddling causes erratic results as MPM is unable to estimate the eigenvalues accurately. However, this can be overcome by processing the samples only after a fault has been detected. Examples of fast fault detection algorithms can be found in [62, 61] and are not part of the current discussion. The faulted SI is estimated at about 0.8 consistently after 5 ms. This classifies the dip under Group 1.

$|V_{10}|$ is estimated at about 0.1 pu and r_{maj} at about 0.9 pu. ϕ_{inc} is estimated at about 60° or -120° as shown in Figure 5.5. Using Table 5.2, we can easily classify this fault under Type E with a A-B ϕ dip correctly using the first 5 ms of sampled data.

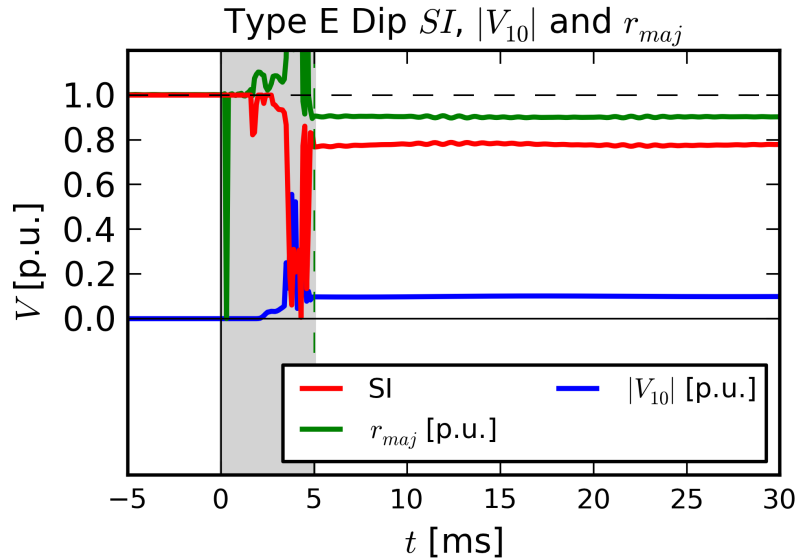


Figure 5.4: Estimated SI , r_{maj} and $|V_{10}|$ for Type E Dip.

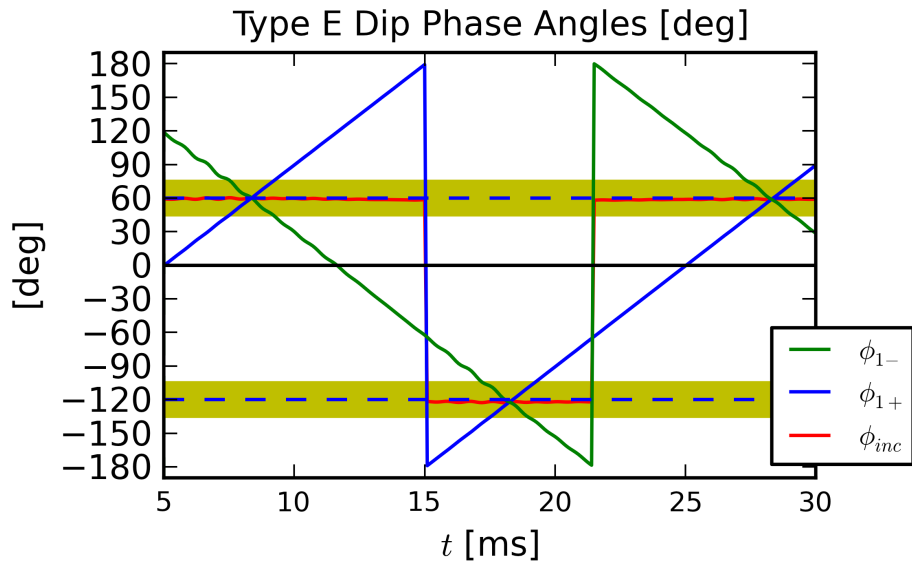


Figure 5.5: Estimated ϕ_{inc} for Type E Dips.

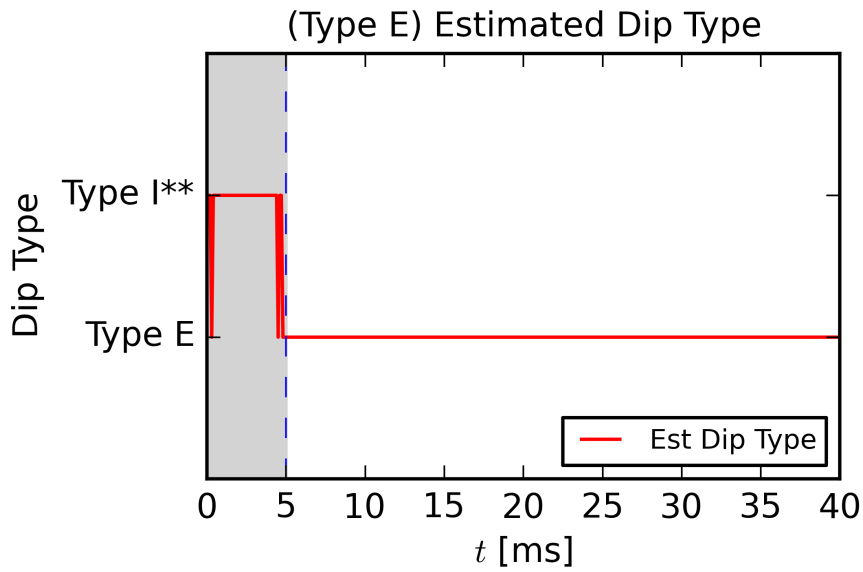


Figure 5.6: Estimated Dip Type for (left) Type C, and (right) Type G Dips.

5.4.3 Summary of Results

We have shown that using MPM on space vectors and zero-sequence voltage, we are able to carry out fault classification on major fault types us-

ing sub-cycle voltage samples. The positive and negative sequence voltage signals can be extracted from the space vectors and used for fault analysis. A distorted fault simulation on simple system has been used to test the proposed method. A sliding sampling window of 5 ms has been used to process the voltage signals. The fault has been correctly classified using the first 5 ms of data or in other words, a quarter cycle time after the fault occurred.

One limitation of MPM fault classification is that it is unable to provide useful information when processing data straddling across faulted and non-faulted region. This means that this method can only be applied after the fault has been detected.

In the next chapter, a more realistic fault classification example using a IEEE-34 standard bus system shall be discussed.

Chapter 6

Modifications to Fault Classification Algorithm

In this chapter, the analysis method described in Chapter 5 shall be more rigorously tested with a realistic case of an IEEE 34-Bus Test System [2]. Subsequently, modifications are made to the original MPM to increase the accuracy and speed of the algorithm. The modifications include augmenting an ellipse fitting algorithm to the MPM method to estimate the parameters of the ellipse and adding a pre-filter and down-sampling process to increase the speed of the algorithm.

6.1 Simulation Setup - IEEE 34-Bus System

To further test the efficacy of using MPM in more realistic situations, two similar and highly distorted faults, ie Type C and Type G dips, have been simulated in a slightly modified IEEE-34 bus test system [2] in Powerfactory [67]. As we can observe from Table 5.2 and 5.3, Type C and G dips are the closest and most difficult to differentiate among the $2-\phi$ dip types. Bollen [4] showed that a Type G dip can be obtained by transforming a

Type E dip via two Dy-transformers consecutively. Hence, buses 854F and 854G have been added with Dy-transformers to the original IEEE-34 bus test system in order to do that. The voltage dips occurred on phases A and B in both cases. The faults were simulated on line 834-842. This is shown in Figure 6.1. The voltage measurements for Type C dip were taken at node 854 while those for Type G were taken at node 854G. The voltage dips at these nodes were less severe than those close to the faulted point and thus were more difficult to differentiate. Type C dip and Type G dip were generated with a phase-to-phase fault and a two-phase-to-ground fault respectively [4].

Fault voltage waveform distortion have been recognized in urban network systems where a mixture of overhead lines and underground cables exist [68], [69]. These distortions increase the difficulty of accurately estimating the fundamental frequency component. The instantaneous phase voltages were sampled at 100 kHz and shown in Figure 6.2. Note that the resulting fault signals look very similar and are highly distorted.

6.1.1 Results of Parameter Estimation with MPM only

It was observed that MPM was able to estimate well the shape of the space vector partial ellipse in the 5 ms sampling window as shown by thick dotted red line in segment (b) in Figure 6.3 even when the recorded signals looks very distorted. However, the estimation becomes poor when the parameters extracted by MPM are used to extrapolate the signal to 20 ms. This is shown by segment (c) in the figure. This poor extrapolation is however resolved by augmenting the MPM with an ellipse fitting algorithm as described in subsequent Subsection 6.1.2. The estimation results of $|V_{10}|$,

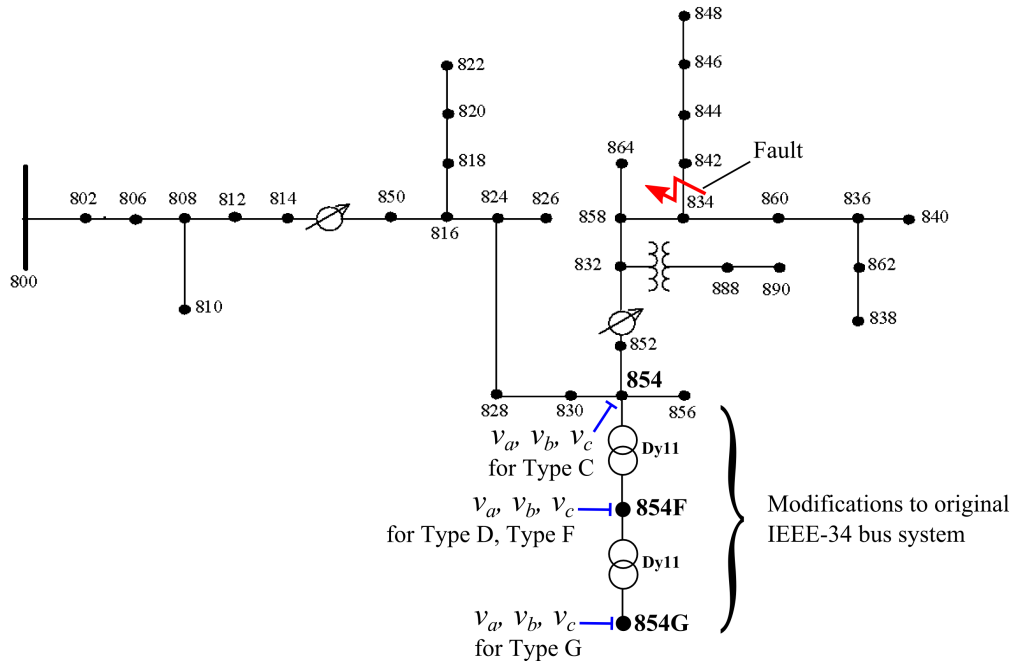


Figure 6.1: Simulated Network

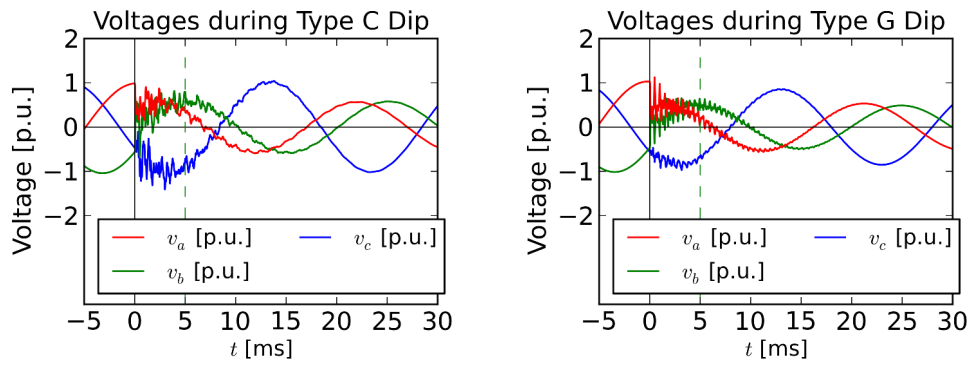


Figure 6.2: Fault voltage waveforms and MPM measured voltages during Type C and G voltage dips.

SI and r_{maj} are shown in Figure 6.5 while those of ϕ_{inc} are shown in Figure 6.4. $|V_{10}|$ was consistently estimated to be below 0.03 pu for both cases but the initial estimates for the other parameters have large fluctuations, causing the classification to be inconsistent until only about 15 ms after the fault has occurred as shown in Figure 6.6. In order to improve this performance, an ellipse fitting algorithm has been augmented as described in the following subsection.

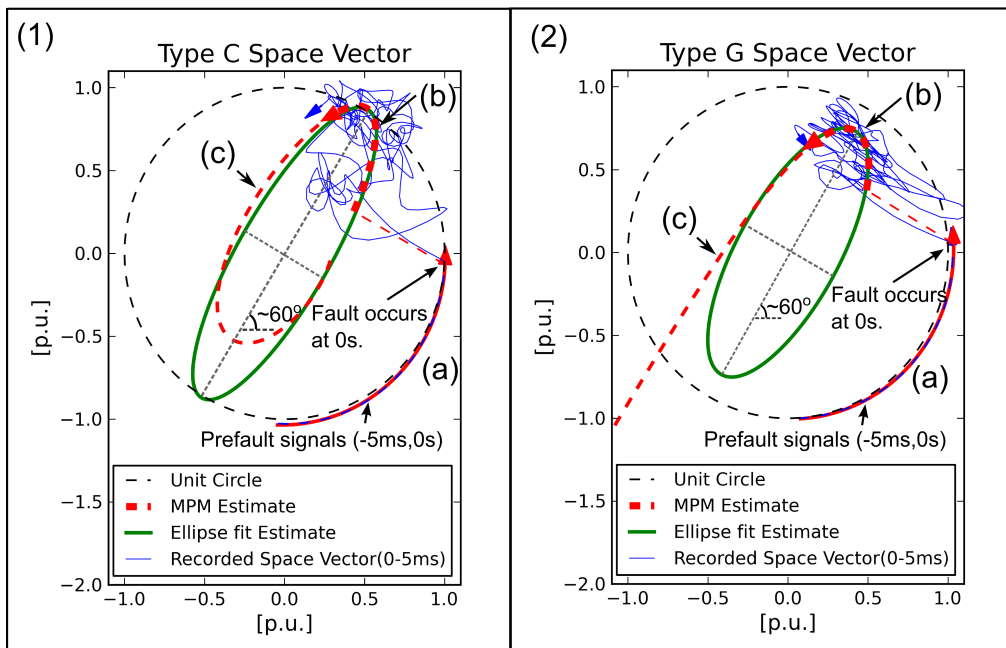


Figure 6.3: Measured voltage space vector, MPM estimated fundamental frequency space vector and MPM with augmented Ellipse fitting estimate for (1) Type C and (2) Type G Dips. Segments (a) and (b) are the MPM estimation from (-5ms, 0s) and (0, 5ms) sampling windows respectively. Segment (c) is the estimated space vector extrapolated to 20 ms based on MPM's results from first 5 ms.

6.1.2 Augmenting with Ellipse Fitting

An efficient yet robust ellipse fitting algorithm [70] has been augmented to improve the estimation performance. With the center coordinates of the

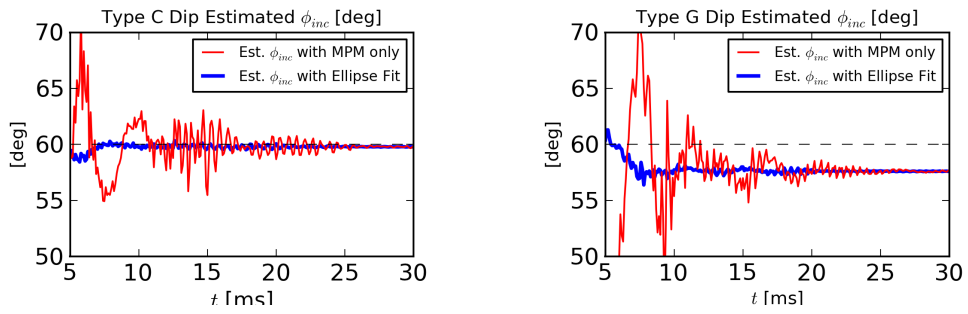


Figure 6.4: Estimated ϕ_{inc} for Type C and G Dips with and without Ellipse fitting.

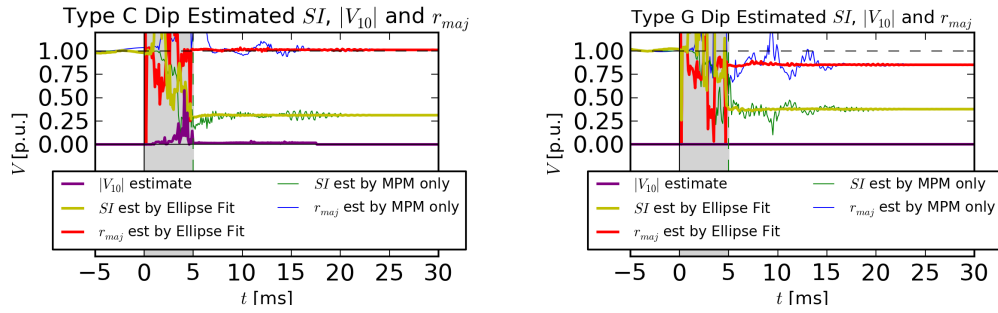


Figure 6.5: Estimated SI and r_{maj} for Type C and G Dips with and without Ellipse fitting.

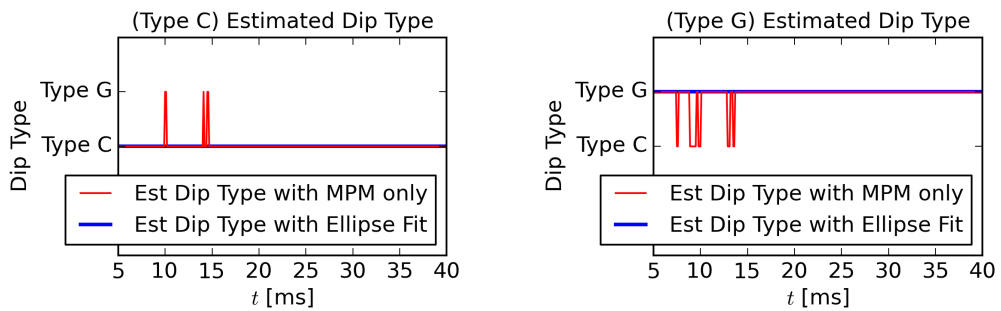


Figure 6.6: Estimated Dip Type for Type C and G Dips with and without Ellipse fitting.

ellipse at (0,0), the equation of an ellipse with three parameters (A, B, γ) is written as:

$$ax^2 + bxy + cy^2 = 1 \quad (6.1)$$

The parameters A, B and γ are shown in Figure 6.7. A is the ellipse's x -axis while B is its y -axis. The ellipse is rotated by angle γ from the original reference axes. The r_{min} and r_{maj} can thus be found by determining which of the A and B values is the major or minor axis. Then ϕ_{inc} can be subsequently be determined from γ easily.

Every three points $[(x_1, y_1), (x_2, y_2), (x_3, y_3)]$ from the partial ellipse can determine a group of the three values of A, B and γ using Equation 6.2 and 6.3. We calculated A, B and γ using every three successive points, 50 samples apart, from MPM's reconstructed 5-ms fundamental frequency space vector and found the medians of A, B and γ from the results. As the three points are 50 samples apart, only 7 groups of samples are used, thus making the computation minimal.

$$a = \frac{\Delta_1}{\Delta_0}, b = \frac{\Delta_2}{\Delta_0}, c = \frac{\Delta_3}{\Delta_0} \quad (6.2)$$

$$\text{where } \Delta_0 = \begin{vmatrix} x_1^2 & x_1y_1 & y_1^2 \\ x_2^2 & x_2y_2 & y_2^2 \\ x_3^2 & x_3y_3 & y_3^2 \end{vmatrix}$$

$$\Delta_1 = \begin{vmatrix} 1 & x_1y_1 & y_1^2 \\ 1 & x_2y_2 & y_2^2 \\ 1 & x_3y_3 & y_3^2 \end{vmatrix}$$

$$\Delta_2 = \begin{vmatrix} x_1^2 & 1 & y_1^2 \\ x_2^2 & 1 & y_2^2 \\ x_3^2 & 1 & y_3^2 \end{vmatrix}$$

$$\Delta_3 = \begin{vmatrix} x_1^2 & x_1y_1 & 1 \\ x_2^2 & x_2y_2 & 1 \\ x_3^2 & x_3y_3 & 1 \end{vmatrix}$$

then

$$\begin{aligned} \gamma &= 0.5 \arctan \frac{b}{a-c} \\ A^2 &= \left| \frac{\cos 2\gamma}{a \cos^2 \gamma - c \sin^2 \gamma} \right| \\ B^2 &= \left| \frac{\cos 2\gamma}{a \sin^2 \gamma - c \cos^2 \gamma} \right| \end{aligned} \quad (6.3)$$

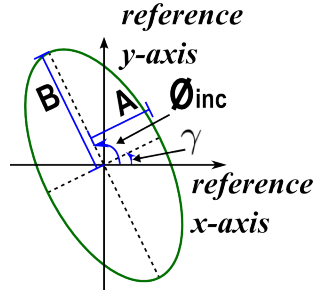


Figure 6.7: Ellipse Parameters

Results

The green line in Figure 6.3 shows the estimated ellipse from the first 5 ms of data after augmenting the fitting algorithm to the MPM method. The results clearly show that this method can greatly improve the estimation of the fundamental frequency space vector ellipse.

The results of the estimation of SI , $|V_{10}|$, r_{maj} and ϕ_{inc} are shown in Figure 6.4 and 6.5. In comparison with those using only MPM method, the augmented technique reduced the fluctuations of the estimated values significantly, enabling the classification to be consistent after 5 ms as shown in Figure 6.6. Using Table 5.2, we can easily classify both faults correctly with the parameters that have been estimated.

6.1.3 Limitations of Current Method

We have shown the use of MPM with augmented ellipse fitting method on voltage dip signal classification. The attentive reader could have recognized that even though this method can analyze the signal with a quarter-cycle length of information, it may involve a relatively long computation time due to the inherent computationally intensive SVD process in MPM. When running this algorithm on an Intel®Core 2™Duo CPU T8300 at 2.4 GHz clock speed with a Microsoft™Windows-XP operating system, the computation time was measured at about 100 to 300 ms depending on whether MPM was also performed on the zero-sequence component or not. The sampling window of the data on the other hand was 5 ms. Hence even though this method can classify the fault using 5 ms of data, the length of computation time would have exceeded 1 fundamental cycle time of 20 ms. This limits the practical use of this method.

Hence, this shall be addressed in the following section where a filtering and down-sampling method is used to process the data before the MPM method in order to reduce computation time.

6.2 Fast Implementation of Fault Classification

The inherent SVD algorithm in MPM is a very computationally intensive process that has a $O(n^3)$ time complexity [71]. Hence, one way to reduce computational time is to reduce the number of samples to be processed by down-sampling the data. However, before the data can be down-sampled, the signal components of frequency higher than the Nyquist frequency of the new sampling rate have to be filtered out to reduce aliasing

effects.

Ideally, the filter should be chosen such that it can effectively attenuate higher frequencies while having minimal transient response. In addition, the filter should also be computationally fast. In our case, slight distortion due to non-linear phase delay is tolerable because only the fundamental frequency component is desired. In view of these requirements, a digital second-order Butterworth filter with a cut-off frequency of 1200 Hz has been chosen. The transient response for the filter to reach steady-state is about 1 ms as shown in Figure 6.8. From the Figure, it can be seen that any increase in the order of the filter will result in a longer time for the filter to reach steady-state. This is undesirable as this would delay the start of MPM processing. MPM can only process the signal after steady-state has been reached so that the desired information can be extracted accurately.

The frequency response of the Butterworth filters are shown in Figure 6.9. Our signals of interest are the fundamental frequency signals that are close to 50 Hz. Figure 6.9 shows that the Butterworth filters have almost no attenuation for signals below 100 Hz and starts to attenuate signals above this frequency. They are thus suitable for our use. A second-order Butterworth filter with a cut-off frequency of 1200 Hz has been chosen as a compromise between its relatively shorter transient response time and greater attenuation of high frequency signals. The filter coefficients has been calculated using the Labview [39] Filters module.

Figure 6.10 shows the resultant frequency plot of the filtered space vector signal of the Type-G dip type previously generated in Subsection 6.1.1 with the modified IEEE 34 Bus network. Frequencies higher than 2.5 kHz are attenuated to lower than -40 dB. With reference to a 1.0 p.u reference signal, -40 dB is equivalent to an amplitude of 0.01 p.u. Recalling Chapter 2, the tolerance setting, tol , for MPM has been set to 0.001 for

data that is accurate up to 3 significant digits. Hence, tol is now set to 0.01 corresponding to -40 dB. As frequencies above 2.5 kHz are attenuated to below -40 dB, down-sampling of the data to a sampling rate of 5 kHz will not cause aliasing effects that adversely affect the feature extraction performance of MPM on 50 Hz signals.

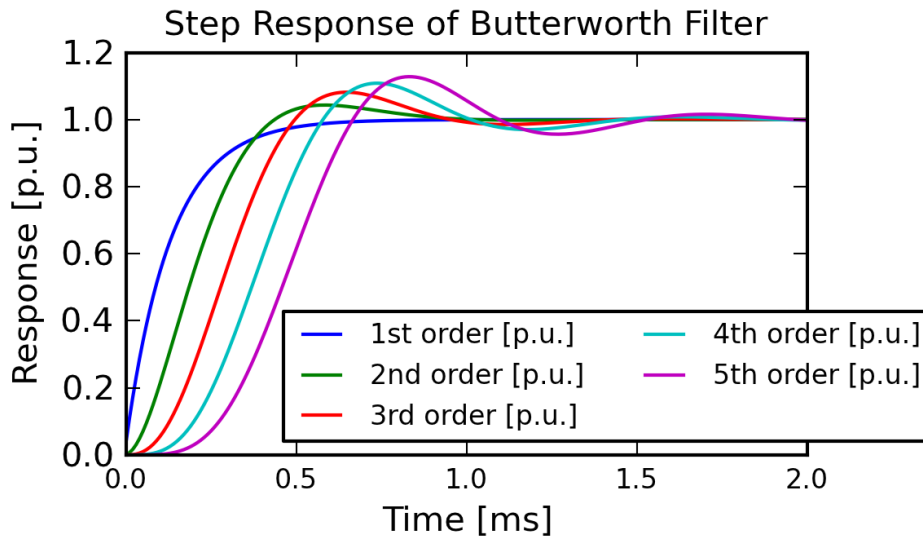


Figure 6.8: Step Response of Low-Pass Butterworth Filter with cut-off frequency at 1200 Hz

As a modification, a sliding window of 600 samples, or equivalently 6 ms, has been used. This is because the first 100 filtered samples shall be discarded as they contain the transient response of the filter. Only the remaining 500 samples are subsequently processed. The remaining filtered samples are then down-sampled by a factor of 20. This reduces the effective sampling rate from 100 kHz to 5 kHz. The number of samples to be processed is also reduced from 500 to 25.

The ellipse fitting-augmented MPM algorithm is then used to process the down-sampled signal to extract the relevant components for fault clas-

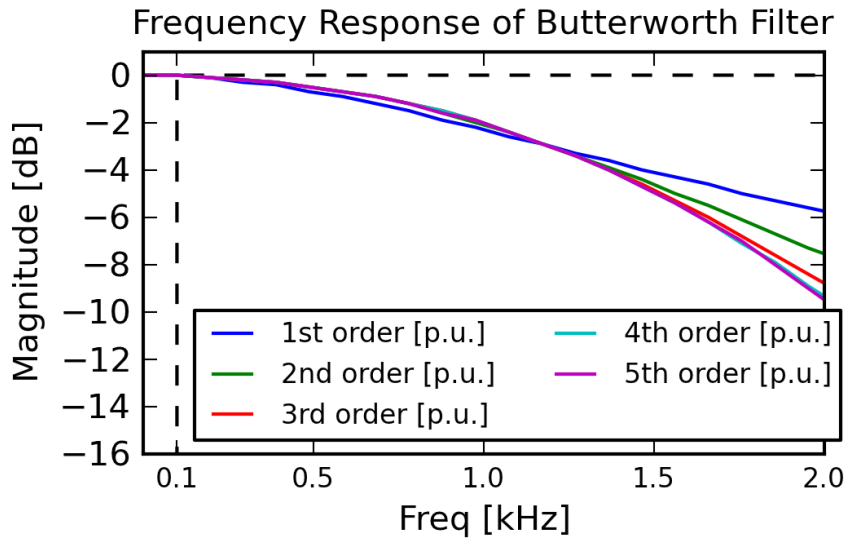


Figure 6.9: Frequency Response of Low-Pass Butterworth Filter with cut-off frequency at 1200 Hz

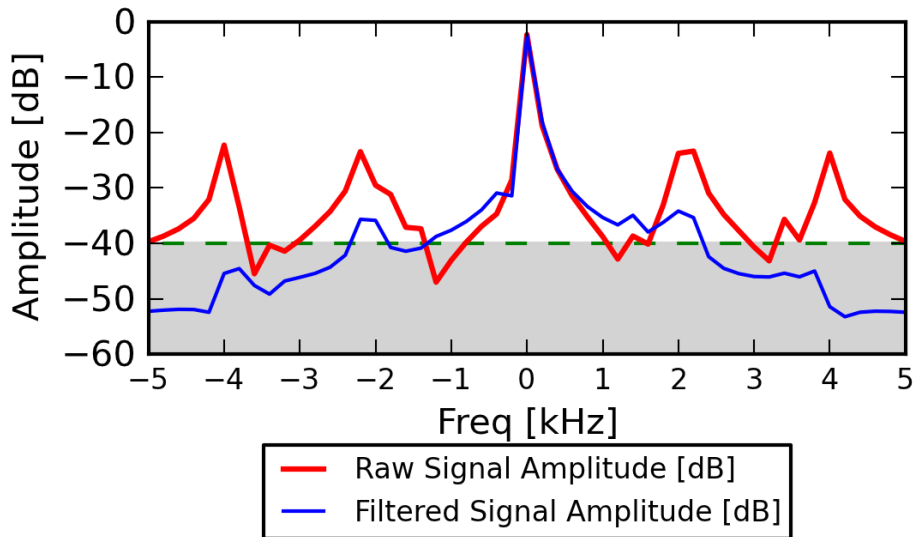


Figure 6.10: Frequency Plot of Raw and Filtered IEEE Case G-Type Dip Space Vector Signal

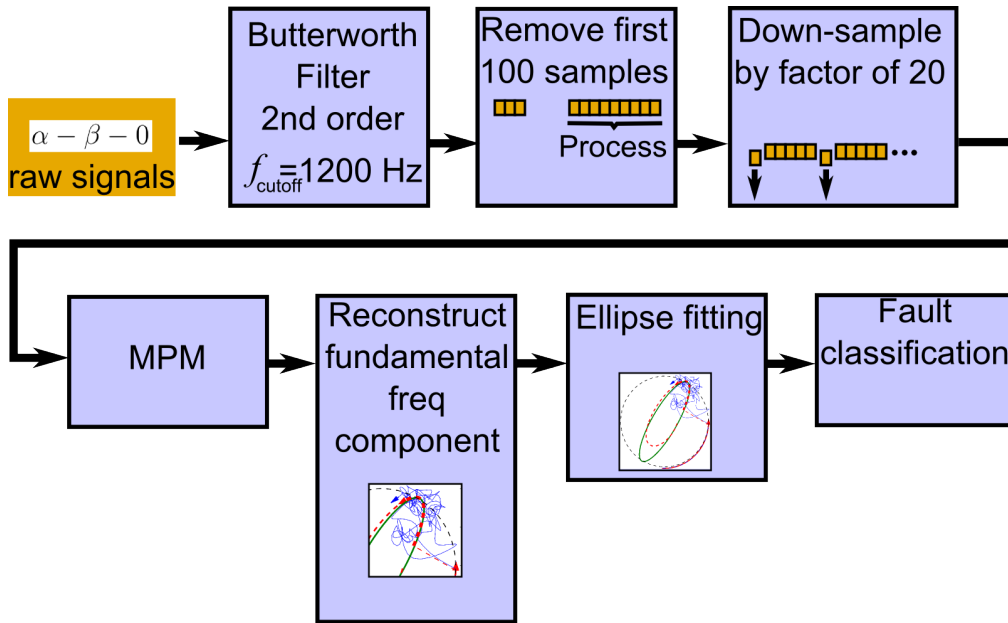


Figure 6.11: Fault Classification Process

sification. The full fault classification process is shown in Figure 6.11.

6.2.1 Simulation and Results

Two similar fault situations are again simulated in the IEEE-34 Bus test system [2] in PowerFactory [67]. A Type D dip and a Type F dip have been generated at node 854F separately by simulating a two-phase and two-phase to ground faults respectively on line 834-842 and transforming them through a Dy11-transformer [4] located between node 854 and 854F. The single line diagram is shown in Figure 6.1. The voltage dips occurred on phase C in both cases. The inclination angle should therefore be approximately -30° according to Table 5.2.

The voltages are sampled at 100 kHz and the fault voltages are shown in Figure 6.12. The fault voltages look very similar and distorted immediately after the onset of the fault.

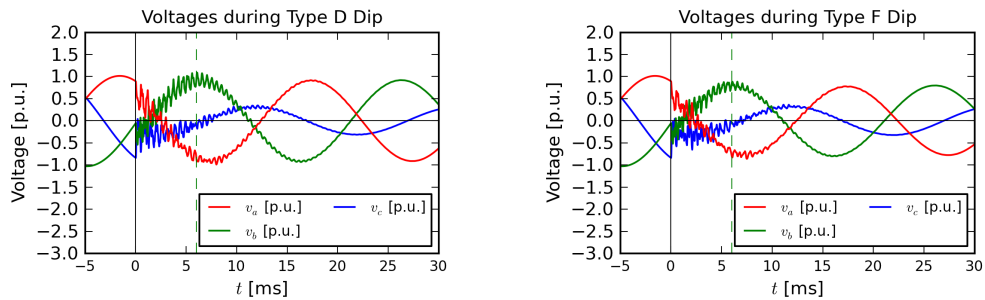


Figure 6.12: Fault voltage waveforms and MPM measured voltages during Type D and F voltage dips.

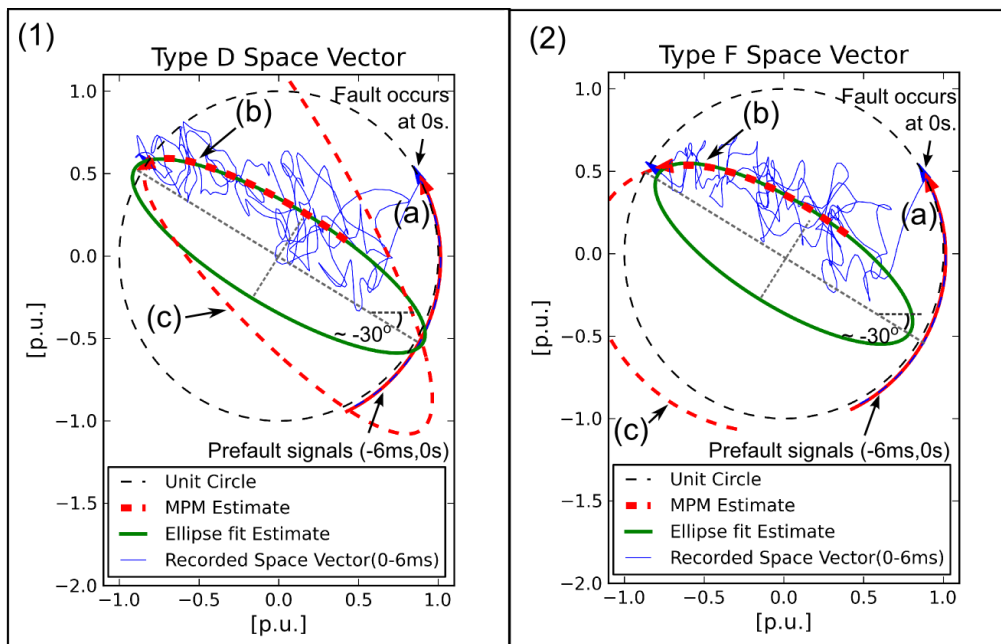


Figure 6.13: Measured voltage space vector, MPM estimated fundamental frequency space vector and MPM with augmented Ellipse fitting estimate for (1) Type D and (2) Type F Dips. Segments (a) and (b) are the MPM estimation from (-6ms, 0s) and (0, 6ms) sampling windows respectively. Segment (c) is the estimated space vector extrapolated to 20 ms based on MPM's results from first 6 ms.

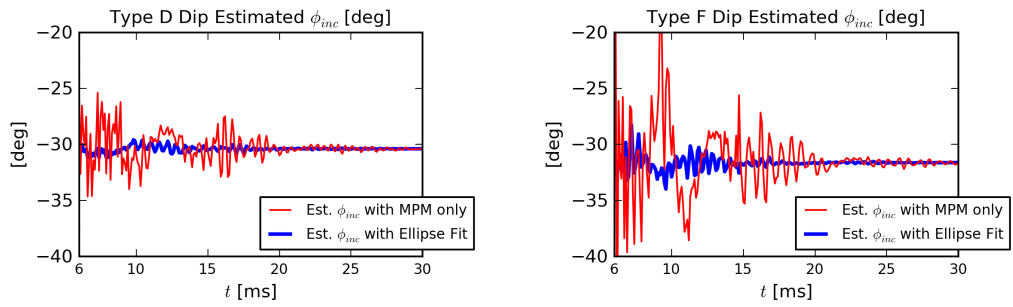


Figure 6.14: Estimated ϕ_{inc} for Type D and F Dips with and without Ellipse fitting.

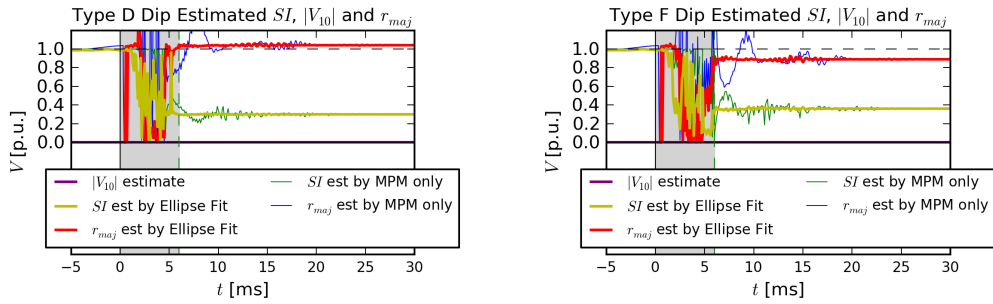


Figure 6.15: Estimated SI and r_{maj} for Type D and F Dips with and without Ellipse fitting.

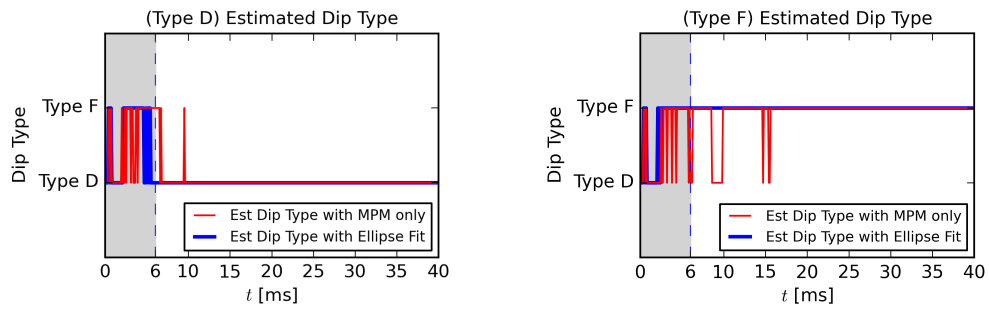


Figure 6.16: Estimated Dip Type for Type D and F Dips with and without Ellipse fitting.

Both the results of using MPM only and the ellipse fit-augmented MPM algorithms have shown in Figure 6.13, 6.14, 6.15 and 6.16.

The results are similar to those of the algorithm used without down-sampling as described in Subsection 6.1.1. Using only MPM, the algorithm was able to estimate well the space vector partial ellipse in the 5 ms sampling window as shown by thick dotted red line in segment (b) in Figure 6.13. However, the estimation becomes poor when the parameters extracted by MPM is used to extrapolate the signal to 20 ms. This is shown by segment (c) in the figure. This poor extrapolation also resulted in inconsistent classification of the fault as shown in Figure 6.16 as the fundamental frequency component parameters were not estimated well. The estimation results of $|V_{10}|$, SI and r_{maj} are shown in Figure 6.15 while those of ϕ_{inc} are shown in Figure 6.14. $|V_{10}|$ was consistently estimated to be below 0.03 pu for both cases.

The green line in Figure 6.13 shows the estimated ellipse from the first 6 ms of data after augmenting the fitting algorithm to the MPM method. The results clearly show that this method greatly improved the estimation of the fundamental frequency space vector ellipse and is minimally affected by the filtering and down-sampling process.

The results of the estimation of SI , $|V_{10}|$, r_{maj} and ϕ_{inc} are shown in Figure 6.14 and 6.15. The ellipse fitting technique reduced the fluctuations of the estimated values significantly, enabling the classification to be consistent after 6 ms from the onset of the fault as shown in Figure 6.16. Using Table 5.2, we can classify both faults correctly with the parameters that have been estimated.

The computation time for running this improved algorithm on an Intel®Core 2™Duo CPU T8300 at 2.4 GHz clock speed with a Microsoft™Windows-XP operating system was measured at about 1 to 3 ms. This meant it is

able to classify the fault by 9 to 10 ms after the onset of the fault. This is an improvement over FFT [1] which required at least 20 ms (1 fundamental cycle) after the fault.

6.3 Summary of Results

We have shown that using MPM on space vectors and zero-sequence components, we are able to carry out fault classification on major voltage dip types using sub-cycle voltage samples. The fundamental frequency positive and negative sequence voltage signals can be extracted from the space vectors and used for fault analysis. An efficient ellipse algorithm has been augmented to MPM for increased accuracy. A highly distorted fault simulation on IEEE-34 distribution bus system has been used to confirm the efficacy of the proposed method. It is shown that a sliding sampling window of 5 ms is sufficient to classify the fault accurately, showing that this method is robust to transients and distortions in the waveform.

This method requires a computation time of 100 to 300 ms which is undesirable. Thus a filtering and down-sampling approach have been used to reduce the computation time. The original signals are passed through the second-order Butterworth filter with a cut-off frequency at 1200 Hz and then down-sampled by a factor of 20. These signals are then processed using the augmented-MPM approach. The results show that this improved technique reduced the computation time to a maximum of 3 ms and still provided consistent and accurate classification results.

Chapter 7

Conclusion and Future Work

7.1 Conclusion

In this thesis, the performance of MPM in relation to sampling window width, sampling frequency and damping factor has been statistically analyzed. It was found that a high sampling frequency does not necessarily yield the best estimation performance of MPM but rather, an optimal sampling frequency should instead be used. MPM is found to be able to estimate the parameters reasonably well between 0.1 to 1 cycle of a moderately damped complex sinusoid.

MPM has been applied to a fault classification technique. This technique performs well on a fault signal generated from a simple theoretical case with a 5 ms sampling window. It is able to extract the fundamental frequency components' parameters consistently and is able to identify a Type E fault well.

In a more realistic fault case in IEEE 34-bus test system, this technique was only able to provide a consistent classification accurately after 15 ms as the estimation of the parameters are affected by the fault transients.

An ellipse fitting algorithm was added to estimate the ellipse parameters

based on fundamental frequency components estimated in the first 5 ms by MPM. This improved the estimation and provided a consistent fault classification using 5 ms of data. This algorithm, however, takes 100 ms to 300 ms of computation which reduces the practical uses of this algorithm.

In order to reduce the computation time, a pre-filtering and down-sampling process have been added. The maximum amount of time for this improved algorithm to complete on an Intel®Core 2™Duo CPU T8300 system is 3 ms. This fast computation thus allows the dip to be classified within 9 to 10 ms from the onset of the dip. This is an improvement from the original method proposed in Vanya [1] that employed FFT to extract the 50 Hz components as that would require a sampling window of at least 20 ms, which is one cycle of the fundamental frequency.

7.2 Future Work

Future work should be done in order to further exploit the use of MPM as a signal processing technique. One example would be to further understand how MPM can improve frequency resolution when there are nearby frequency components near the frequency of interest. This would aid in the feature extraction performance in such situations.

Other applications of MPM in power systems analysis can also be researched on as part of the future work. All in all, MPM has been shown to be a promising method of feature extraction. Further work should be done to fully exploit its uses in the power system signal analysis.

Bibliography

- [1] V. Ignatova, P. Granjon and S. Bacha, “Space Vector Method for Voltage dips and Swells Analysis,” *IEEE Transactions on Power Delivery*, vol. 24, no. 4, pp. 2054–2061, Oct 2009.
- [2] “IEEE distribution system analysis subcommittee, IEEE 34 node test feeder,” <http://ewh.ieee.org/soc/pes/dsacom/testfeeders.html>, Accessed: 31/12/2012.
- [3] Jan Machowski, Janusz Bialek, and Jim Bumby, “Introduction,” in *Power System Dynamics: Stability and Control*, chapter 1. John Wiley and Sons, 2008.
- [4] Math H. Bollen, “Voltage sags - characterization,” in *Understanding Power Quality Problems: Voltage Sags and Interruptions*, chapter 4. Wiley, 2000.
- [5] H. Farhangi, “The path of the smart grid,” *Power and Energy Magazine, IEEE*, vol. 8, no. 1, pp. 18 –28, january-february 2010.
- [6] S. Grenard, O. Devaux, O. Carre, and O. Huet, “Power steering,” *Power and Energy Magazine, IEEE*, vol. 9, no. 5, pp. 42 –51, sept.-oct. 2011.
- [7] J. D. L. Ree, V. Centeno, J. S. Thorp, and A. G. Phadke, “Syn-

- chronized phasor measurement applications in power systems,” *IEEE Transactions on Smart Grid*, vol. 1, no. 1, pp. 20–27, June 2010.
- [8] Guoping Liu, J. Quintero, and V. Venkatasubramanian, “Oscillation monitoring system based on wide area synchrophasors in power systems,” in *Bulk Power System Dynamics and Control - VII. Revitalizing Operational Reliability, 2007 iREP Symposium*, aug. 2007, pp. 1–13.
- [9] J. L. Suonan, Y. Zhong, and G. B. Song, “A novel distance protection algorithm in frequency domain based on parameter identification,” in *Developments in Power Systems Protection, 2012. DPSP 2012. 11th International Conference on*, april 2012, pp. 1–6.
- [10] Xin hui Zhang, Shu xian Fan, Hao Duan, and Bing yin Xu, “Analysis of transient dominant frequency signal for single-phase earthed fault based on prony algorithm,” in *Electricity Distribution, 2008. CICED 2008. China International Conference on*, dec. 2008, pp. 1–6.
- [11] R. Mardiana, H.A. Motairy, and C.Q. Su, “Ground fault location on a transmission line using high-frequency transient voltages,” *Power Delivery, IEEE Transactions on*, vol. 26, no. 2, pp. 1298–1299, april 2011.
- [12] A. Borghetti, M. Bosetti, M. Di Silvestro, C.A. Nucci, and M. Paolone, “Continuous-wavelet transform for fault location in distribution power networks: Definition of mother wavelets inferred from fault originated transients,” *Power Systems, IEEE Transactions on*, vol. 23, no. 2, pp. 380–388, may 2008.
- [13] A. Ametani and T. Kawamura, “A method of a lightning surge analy-

- sis recommended in japan using emtp,” *Power Delivery, IEEE Transactions on*, vol. 20, no. 2, pp. 867 – 875, april 2005.
- [14] C.I. Chen and G.W. Chang, “An efficient time-domain approach based on prony’s method for time-varying power system harmonics estimation,” in *Power Energy Society General Meeting, 2009. PES ’09. IEEE*, july 2009, pp. 1 –6.
- [15] P. Kundur, *Power System Stability and Control*, McGraw-Hill, 1994.
- [16] “Dynamic models for combined cycle plants in power system studies,” *Power Systems, IEEE Transactions on*, vol. 9, no. 3, pp. 1698 –1708, aug 1994.
- [17] Bo Lu and M. Shahidehpour, “Short-term scheduling of combined cycle units,” *Power Systems, IEEE Transactions on*, vol. 19, no. 3, pp. 1616 – 1625, aug. 2004.
- [18] M. Jordan, H. Langkowski, Trung Do Thanh, and D. Schulz, “Frequency dependent grid-impedance determination with pulse-width-modulation-signals,” in *Compatibility and Power Electronics (CPE), 2011 7th International Conference-Workshop*, june 2011, pp. 131 –136.
- [19] H. Langkowski, Trung Do Thanh, K.-D. Dettmann, and D. Schulz, “Grid impedance determination; relevancy for grid integration of renewable energy systems,” in *Industrial Electronics, 2009. IECON ’09. 35th Annual Conference of IEEE*, nov. 2009, pp. 516 –521.
- [20] Xin Chen and Jian Sun, “A study of renewable energy system harmonic resonance based on a dg test-bed,” in *Applied Power Electronics Conference and Exposition (APEC), 2011 Twenty-Sixth Annual IEEE*, march 2011, pp. 995 –1002.

- [21] F.A.S. Neves, H.E.P. de Souza, F. Bradaschia, M.C. Cavalcanti, M. Rizo, and F.J. Rodriguez, “A space-vector discrete fourier transform for unbalanced and distorted three-phase signals,” *Industrial Electronics, IEEE Transactions on*, vol. 57, no. 8, pp. 2858–2867, aug. 2010.
- [22] A.J.F. Hauer, D.J. Trudnowski, and J.G. DeSteele, “A perspective on WAMS analysis tools for tracking of oscillatory dynamics,” in *Power Engineering Society General Meeting, 2007. IEEE*, june 2007, pp. 1–10.
- [23] R. Yan and R.X. Gao, “Tutorial 21 wavelet transform: a mathematical tool for non-stationary signal processing in measurement science part 2 in a series of tutorials in instrumentation and measurement,” *Instrumentation Measurement Magazine, IEEE*, vol. 12, no. 5, pp. 35–44, october 2009.
- [24] Wenxian Yang, P.J. Tavner, C.J. Crabtree, and M. Wilkinson, “Cost-effective condition monitoring for wind turbines,” *Industrial Electronics, IEEE Transactions on*, vol. 57, no. 1, pp. 263–271, jan. 2010.
- [25] M. Khan and M.A. Rahman, “Development and implementation of a novel fault diagnostic and protection technique for ipm motor drives,” *Industrial Electronics, IEEE Transactions on*, vol. 56, no. 1, pp. 85–92, jan. 2009.
- [26] K. Teotrakool, M.J. Devaney, and L. Eren, “Adjustable-speed drive bearing-fault detection via wavelet packet decomposition,” *Instrumentation and Measurement, IEEE Transactions on*, vol. 58, no. 8, pp. 2747–2754, aug. 2009.

- [27] J. Turunen, T. Rauhala, and L. Haarla, “Selecting wavelets for damping estimation of ambient-excited electromechanical oscillations,” in *Power and Energy Society General Meeting, 2010 IEEE*, july 2010, pp. 1 –8.
- [28] J. Turunen, L. Haarla, and T. Rauhala, “Performance of wavelet-based damping estimation method under ambient conditions of the power system,” in *Bulk Power System Dynamics and Control (iREP) - VIII (iREP), 2010 iREP Symposium*, aug. 2010, pp. 1 –9.
- [29] J. Slavic and M Boltezar, “Damping identification with the morlet-wave,” in *Mechanical Systems and Signal Processing*, jul. 2011, vol. 25, pp. 1632 –1645.
- [30] J.F. Hauer, C.J. Demeure, and L.L. Scharf, “Initial results in prony analysis of power system response signals,” *Power Systems, IEEE Transactions on*, vol. 5, no. 1, pp. 80 –89, feb 1990.
- [31] T.K. Sarkar and O. Pereira, “Using the matrix pencil method to estimate the parameters of a sum of complex exponentials,” *Antennas and Propagation Magazine, IEEE*, vol. 37, no. 1, pp. 48 –55, feb 1995.
- [32] Y. Hua and T.K. Sarkar, “Matrix pencil method for estimating parameters of exponentially damped/undamped sinusoids in noise,” *Acoustics, Speech and Signal Processing, IEEE Transactions on*, vol. 38, no. 5, pp. 814 –824, may 1990.
- [33] L.L. Grant and M.L. Crow, “Comparison of matrix pencil and prony methods for power system modal analysis of noisy signals,” in *North American Power Symposium (NAPS), 2011*, aug. 2011, pp. 1 –7.

- [34] P Ribeiro, “Prony analysis for time-varying harmonics,” in *Time-Varying Waveform Distortions in Power Systems*, chapter 25. Wiley-IEEE Press, 1 edition, 2010.
- [35] T. Lobos, Z. Leonowicz, J. Rezmer, and P. Schegner, “High-resolution spectrum-estimation methods for signal analysis in power systems,” *Instrumentation and Measurement, IEEE Transactions on*, vol. 55, no. 1, pp. 219 – 225, feb. 2006.
- [36] M.S. Reza, M. Ciobotaru, and V.G. Agelidis, “Power quality analysis using piecewise adaptive prony’s method,” in *Industrial Technology (ICIT), 2012 IEEE International Conference on*, march 2012, pp. 926 –931.
- [37] M.L. Shelton, P.F. Winkelman, W.A. Mittelstadt, and W. J. Bellerby, “Bonneville power administration 1400-mw braking resistor,” *Power Apparatus and Systems, IEEE Transactions on*, vol. 94, no. 2, pp. 602–611, 1975.
- [38] G. H. Golub and C. F. V. Loan, “Orthogonalization and least squares,” in *Matrix Computations*, chapter 5. John Hopkins, 3 edition, 1996.
- [39] “<http://www.ni.com/labview/>,” Jan 2013.
- [40] José Enrique Fernández del Río and Tapan K Sarkar, “Comparison between the matrix pencil method and the fourier transform technique for high-resolution spectral estimation,” in *Digital Signal Processing*, April 1996, vol. 6, pp. 108–125.
- [41] El-Hadi Djermoune and Marc Tomczak, “Statistical analysis of the kumaresan-tufts and matrix pencil methods in estimating a damped

- sinusoid,” in *European Signal Processing Conference*, September 2004, pp. 1261–1264.
- [42] Michel Meunier and Francoise Brouaye, “Fourier transform, Wavelets, Prony analysis: Tools for Harmonics and Quality of Power,” in *8th International Conference on Harmonics and Quality of Power*, 1998, vol. 1, pp. 71–76.
- [43] Rik Pintelon and Johans Schoukens, “Some probability and stochastic convergence fundamentals,” in *System Identification: A Frequency Domain Approach*, chapter 14. IEEE Press, 1 edition, 2001.
- [44] “<http://www.python.org/download/releases/2.7.3/>,” July 2013.
- [45] “<https://www.enthought.com/products/epd/free/>,” July 2013.
- [46] “http://matplotlib.org/mpl_toolkits/mplot3d/api.html,” July 2013.
- [47] “<http://www.scipy.org/>,” July 2013.
- [48] “<http://www.numpy.org/>,” July 2013.
- [49] O. Ipinnimo, S. Chowdhury, and S.P. Chowdhury, “Voltage dip mitigation with DG integration: A comprehensive review,” in *Power Electronics, Drives and Energy Systems (PEDES) 2010 Power India, 2010 Joint International Conference on*, dec. 2010, pp. 1–10.
- [50] D. Ezer, R.A. Hanna, and J. Penny, “Active voltage correction for industrial plants,” *Industry Applications, IEEE Transactions on*, vol. 38, no. 6, pp. 1641–1646, nov/dec 2002.
- [51] B. Kasztenny, I. Voloh, C.G. Jones, and G. Baroudi, “Detection of incipient faults in underground medium voltage cables,” in *Protective*

- Relay Engineers, 2008 61st Annual Conference for*, april 2008, pp. 349–366.
- [52] *SEMI F47-0200 Specification for Semiconductor Processing Equipment Voltage Sag Immunity*, Semiconductor Equipment and Materials International, 1999/2000.
- [53] Olivier Carré Sébastien Grenard, Olivier Devaux and Olivier Huet, “Power steering,” in *IEEE Power & Energy Magazine*, Sep/Oct 2011, pp. 42–51.
- [54] C. L. Fortescue, “Method of symmetrical co-ordinates applied to the solution of polyphase networks,” *American Institute of Electrical Engineers, Transactions of the*, vol. XXXVII, no. 2, pp. 1027–1140, july 1918.
- [55] R.A. Flores, I.Y.H. Gu, and M.H.J. Bollen, “Positive and negative sequence estimation for unbalanced voltage dips,” in *Power Engineering Society General Meeting, 2003, IEEE*, july 2003, vol. 4, p. 4 vol. 2666.
- [56] G.M.S. Azevedo, F.A.S. Neves, M.C. Cavalcanti, L.R. Limongi, and F. Bradaschia, “Fault detection system for distributed generation converters,” in *Power Electronics Conference (COBEP), 2011 Brazilian*, sept. 2011, pp. 320–327.
- [57] C.J. Kim and T.O. Bialek, “Sub-cycle ground fault location; formulation and preliminary results,” in *Power Systems Conference and Exposition (PSCE), 2011 IEEE/PES*, march 2011, pp. 1–8.
- [58] L.A. Kojovic and Jr. Williams, C.W., “Sub-cycle detection of incipient cable splice faults to prevent cable damage,” in *Power Engineering*

- Society Summer Meeting, 2000. IEEE*, 2000, vol. 2, pp. 1175 –1180
vol. 2.
- [59] W. C. Duesterhoeft, Max W. Schulz, and Edith Clarke, “Determination of instantaneous currents and voltages by means of alpha, beta, and zero components,” *American Institute of Electrical Engineers, Transactions of the*, vol. 70, no. 2, pp. 1248 –1255, july 1951.
- [60] O. Poisson, P. Rioual, and M. Meunier, “Detection and measurement of power quality disturbances using wavelet transform,” *Power Delivery, IEEE Transactions on*, vol. 15, no. 3, pp. 1039 –1044, jul 2000.
- [61] M.A.S. Masoum, S. Jamali, and N. Ghaffarzadeh, “Detection and classification of power quality disturbances using discrete wavelet transform and wavelet networks,” *Science, Measurement Technology, IET*, vol. 4, no. 4, pp. 193 –205, july 2010.
- [62] Emmanouil Styvaktakis, *Automating Power Quality Analysis*, Ph.D. thesis, Chalmers University of Technology, 2002.
- [63] Yoshihide Hase, “The α - β -0 coordinate method (clarke components) and its application,” in *Handbook of Power System Engineering*, chapter 6. Wiley, 2007.
- [64] Guibin Zhang and Zheng Xu, “A new real-time negative and positive sequence components detecting method based on space vector,” in *Power Engineering Society Winter Meeting, 2001. IEEE*, jan-1 feb 2001, vol. 1, pp. 275 –280 vol.1.
- [65] “ENTSO-E network code for requirements for grid connection applicable to all generators,” https://www.entsoe.eu/fileadmin/user_upload/

_library/resources/RfG/130308_Final_Version_NC_RfG.pdf, Accessed: 20/06/2013.

- [66] “IEEE recommended practice for evaluating electric power system compatibility with electronic process equipment,” *IEEE Std 1346-1998*.
- [67] “<http://www.digsilent.de/index.php/products-powerfactory.html>,” Jan 2013.
- [68] Yoshihide Hase, *Handbook of Power System Engineering*, Wiley, 2007.
- [69] Y. Ohura, T. Matsuda, M. Suzuki, M. Yamaura, Y. Kurosawa, and T. Yokoyama, “Digital distance relay with improved characteristics against distorted transient waveforms,” *Power Delivery, IEEE Transactions on*, vol. 4, no. 4, pp. 2025–2031, oct 1989.
- [70] Wei Wen and Baozong Yuan, “Detection of partial ellipses using separate parameters estimation techniques,” in *Proceedings of the British Machine Vision Conference*. 1994, pp. 25.1–25.10, BMVA Press, doi:10.5244/C.8.25.
- [71] P. B. Richard, T.L. Franklin, and V.L. Charles, “Computation of the singular value decomposition using mesh-connected processors,” *Journal of VLSI and Computer Systems*, vol. 1, no. 3, pp. 242 – 270, 1983-5.